Assessment of Near-Angle Scatter on Exo-Earth Coronagraphy

H. Philip Stahl,[a] Bijan Nemati,[b] Manuel Quijada,[c] Luis Rodriguez,[d] Javier Del Hoyo,[c] Scott Ellis[e]
[a]NASA Marshall Space Flight Center, Huntsville, AL 35812, U.S.A.
[b]Tellus1 Scientific, LLC, Huntsville, AL 35802, U.S.A.
[c]NASA Goddard Space Flight Center, Greenbelt, MD 20771, U.S.A.
[d]CUA and NASA Goddard Space Flight Center (CRESST II), Greenbelt, MD 20771, U.S.A.
[e]Photon Engineering, Tucson, AZ 85711, U.S.A.

Abstract

Near-Angle Scatter (NAS) of the host star's light into the coronagraph dark hole may limit the ability of a potential Habitable Worlds Observatory (HWO) to detect and characterize an Earth-like planet around a Sun-like star. This paper summarizes a 5-year investigation of the impact of NAS on high-contrast coronagraphy. Science requirements were flowed down to a draft flux ratio noise ratio (FRN) error budget with allocations for NAS. The modeled sources of NAS include correlated (low and mid-spatial) surface structure, uncorrelated surface microroughness and coating structure, particulate contamination, micrometeoroid impacts and polarization leakage.

The paper develops specifications for these sources of scattered light that meet their FRN error budget allocations, distinguishing between scatter that can and cannot be modulated. The development process utilizes an analytical expression that predicts scatter throughput into the dark hole based on BRDF/BSDF. Using this relationship, Photon Engineering performed a FRED® straylight analysis of the HWO EAC-1 (Exploratory Analytical Case #1) coronagraph to parametrically study predicted scattered light contrast in the dark hole. The model revealed that primary mirror microroughness or contamination is not a significant source of scattered light; the most critical surfaces are the smallest and those located closest to the coronagraph focal plane mask. The assessment found that uncorrelated microstructure, contamination, and micrometeoroid impacts require more investigation and potential significant sources of unmodulated scattered

light, and highlights that slow thermal wavefront drift is an order of magnitude more impactful than fast mechanical jitter.

Keywords: near-angle scattered light, angular scatter, diffuse scatter, error budget, contamination, micrometeoroid impact, coronagraphy

1 Introduction

The National Academy Decadal Survey on Astronomy and Astrophysics 2020 [1] prioritized an ~ $11B mission (life cycle cost) to characterize ~ 25 Earth-like planets located in a greater than 60 milli-arc-second (mas), or 0.000017 degrees, orbit (nominal) from their Sun-like stars using a coronagraph. Because Earth-like planets are small, they are typically ~1E-10 fainter than their host star. To see an Earth-like planet, its host star's light must be suppressed by a factor of a few million relative to the host star's point spread function intensity at the planet's location.

In the summer of 2021, before his death in 2022, Dr. James Breckinridge asked Dr. H. Philip Stahl to look into "how near-angle scatter might impact exo-Earth coronagraphy". Based on his 2018 paper [2], Dr. Breckinridge was concerned that near-angle scatter of a host star's light from mirror surface microroughness and particulate contamination "may hopelessly overwhelm" the ability to detect and characterize a potential exo-Earth located 50 to 100 milli-arc-seconds (mas) from its host star – making exo-Earth science via coronagraphy impossible.

Additionally, it was noted that no coronagraph testbed has yet achieved its theoretical performance limit. [3-5] All test beds have been limited by a signal that cannot be modulated, i.e. a signal that cannot be reduced via a deformable mirror and the process of electric field conjugation (EFC). One hypothesized cause of this unmodulated contrast is near-angle scatter.

A review of the literature determined that, while 'near-angle scatter' is a well-known phenomenon, no previous mission had needed to determine the amplitude of near-angle scatter irradiance at an angular separation of 50 to 100 mas from specular. Thus, the risk to exo-Earth coronagraphic science had not been previously investigated. The Exoplanet Exploration Program Office (ExEP) concurred with this risk assessment and endorsed a study. After ExEP briefed Astrophysics Division (APD), a request for an assessment was submitted to and approved by the NASA Engineering and Safety Center (NESC).

The NESC assessment was conducted using a science-driven systems-engineering methodology. A team of subject matter experts (SMEs) from relevant disciplines (systems engineering, coronagraphy, straylight, coating, micrometeoroid, etc.) was assembled to derive physical optical surface parameter specifications from science requirements.

A raw contrast error budget was developed for characterizing Earth-like planets around Sun-like stars and allocations assigned to sources of near-angle scatter (NAS), including but not limited to correlated surface structure, uncorrelated microroughness, coating structure, contamination, micrometeoroid impacts and polarization. **[6-7]** Diffraction from segment edges and ghost reflections were beyond the scope of this assessment. Specifications for correlated surface structure and roughness were derived from the error budget contrast allocations using Rayleigh-Rice Vector Scatter Theory **[8-11]** and Generalized Harvey-Shack Scalar Scatter Theory. **[2, 8-11]** These specifications are completely consistent with specifications developed by others **[12-16]** and serve to validate the scatter theory methodology.

An analytical relationship was derived between coronagraph contrast and Bidirectional Reflectance Distribution Function (BRDF) **[7, 10-11]** – sometimes also referred to as BSDF for 'scatter'. This flowed naturally to a relationship between coronagraph contrast and wavefront Power Spectral Density (PSD). **[7, 8]** Using these relationships, a parametric straylight analysis was conducted of the Habitable Worlds Observatory (HWO) Exploratory Analytical Case #1

(EAC-1) coronagraph as a function of optical surface PSD (correlated and uncorrelated structure), microroughness, contamination and polarization using Photon Engineering's FRED® software. [7] Three different PSD models were used for the FRED® analysis. The first was provided by ExEP. The other two were derived from measurements of candidate HWO reflectance coating performed by the Goddard Space Flight Center (GSFC) Coating Lab. Again, the FRED® results are consistent with diffraction propagation modeling of others. [17-18]

This paper summarizes 5 years of development and analysis.

2 Science Requirement Drives Specifications

Direct imaging of exoplanets requires coronagraph/telescope systems capable of rejecting the light from the host star to below the brightness of its companions. The potential Habitable Worlds Observatory (HWO) desires to detect and characterize Earth-like planets in the habitable zone of nearby Sun-like stars. Viewed at a distance of 10-parsecs, such planets would have a maximum angular separation of 100 mas (0.1″) (Fig 1). As detailed in Appendix A, the flux ratio (i.e. ratio of planet's reflected light to its host star's direct light) for an Earth-like planet at an 80-degree phase angle is 150 ppt (part-per-trillion). HWO proposes to achieve this flux ratio with a coronagraph (Fig 2).

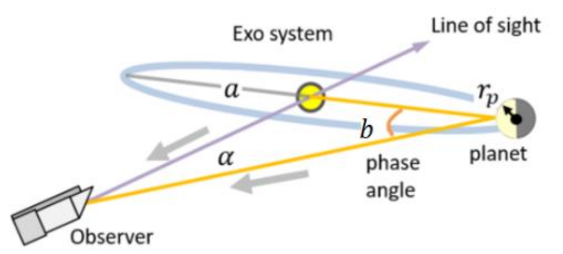

Fig. 1: The flux ratio of an exoplanet depends on its radius, orbital semi-major axis, and the phase angle.

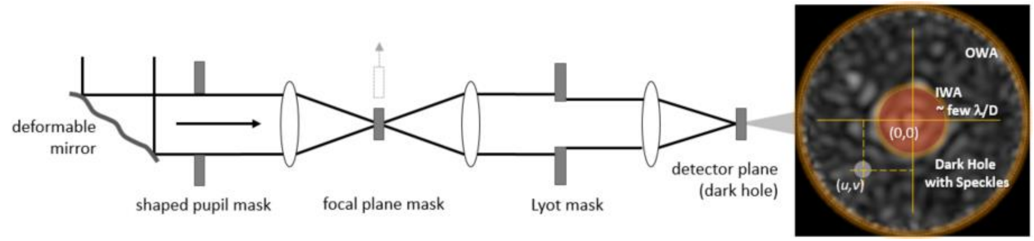

Fig. 2: Typical coronagraph: incoming light from the left is shaped in phase by a deformable mirror (or in phase and amplitude by two separated deformable mirrors), then sent through a focal plane and Lyot mask. The result is a 'dark hole' where (on-axis) starlight is strongly suppressed relative to the (off-axis) planet light. The inner and outer working angles (IWA, OWA, respectively, denote the limits of the coronagraph suppression region.

Coronagraphs achieve this flux ratio by blocking the star's light with a focal plane mask (FPM). The planet's light, which comes in at a slight angle, misses this mask and proceeds. After recollimation, a 'Lyot' mask removes most (but not all) of the remaining on-axis light. The beam is then focused onto the detector, creating what is usually referred to as a 'dark hole,' a zone where host star light has been strongly suppressed. The key attributes of any coronagraph needed to derive a direct-imaging error budget are core throughput, inner and outer working angles, and raw contrast. [12] For the NAS study, the key parameter is contrast.

Contrast is the measure of coronagraph's ability to achieve a given flux ratio. Contrast is defined as the ratio of two throughputs (see Fig 2 for coordinates):

$$C(u,v) \equiv \frac{\tau\,(u,v)}{\tau_{pk}\,(u,v)}\,,$$

where $\tau_{pk}(u,v)$ is the "peak" throughput or fraction of the star's light, if it were located at (u,v), detected within a solid angle region of interest Ω_r centered at (u,v) relative to the total light incident upon the primary mirror. And $\tau(u,v)$ is defined as the ratio of power at position (u,v) divided by total incident power from the star, in its nominal position of (0,0).

$$\tau(u,v) \equiv \frac{\Phi\,(u,v)}{\Phi_i\,(0,0)}\,,$$

If a coronagraph were perfect, then $\tau(u,v)$ would be zero and $\tau_{pk}\ (u,v)$ would be 1. But coronagraphs are not perfect. Even after wavefront control gives the coronagraph its final level of starlight suppression, a small amount of light (E-field) will 'leak' around the coronagraph mask due to design inefficiency and wavefront instability. The contribution of this light to the dark hole is quantified by the speckle throughput, τ_{sp}. Our study identifies another leakage source, near-angle scatter (NAS), which is quantified by NAS throughput, τ_{NAS}. NAS is largely coherent – electric field diffracted by correlated spatial surface structure. But NAS also has an incoherent contribution caused by uncorrelated spatial structure. Other potential leakage sources include polarization retardance. Total throughput is the sum of all sources:

$$\tau(u,v) = \tau_{\mathrm{sp}} + \tau_{\mathrm{NAS}} + \ldots$$

The importance of the 'leaked' E-field is that it produces a speckle intensity pattern given in the dark hole. The dark hole speckle intensity is described by $|E(u,v)|^2$. Disturbance or drift error in the opto-mechanical configuration of the telescope or coronagraph produces small changes in the E-field. These changes coherently add a perturbation field $\Delta E(u,v,t)$ to the 'initial' or 'static' part of the field $E(u,v)$. Coherent mixing of the original field E and perturbation field ΔE creates a temporally dynamic speckle pattern, the intensity of which is given by:

$$|E + \Delta E|^2 = |E|^2 + |\Delta E|^2 + 2\,\mathcal{R}\{E^* \cdot \Delta E\} \qquad \text{[Eq 1]}$$

It is the $2\,\mathcal{R}\{E^* \cdot \Delta E\}$ mixing term which maps into an error budget's residual speckle allocation. Typical error budgets assume that the static E-field is entirely caused by coronagraph mask inefficiency when deriving a wavefront instability specification. But near-angle scatter can increase the static E-field. Consequently, to keep the heterodyne mixing term constant, the allowed wavefront instability ΔE must become smaller. Also, if NAS increases the static E-field, then it increases the $|E|^2$ shot noise.

As described in Appendix A, this paper following a methodology described in detail by Nemati et al. **[19]** allocate flux ratio into a top-level Flux Ratio Noise (FRN) error budget. Figure 3 shows a complete FRN error budget and one potential sub-allocation of this top-level error budget into modulated (coherent) and unmodulated (incoherent) noise contributions. Also, as discussed in Appendix A, this error budget will be 7X smaller for an exo-planet with a limiting case flux ratio of 33 ppt. **[20]**

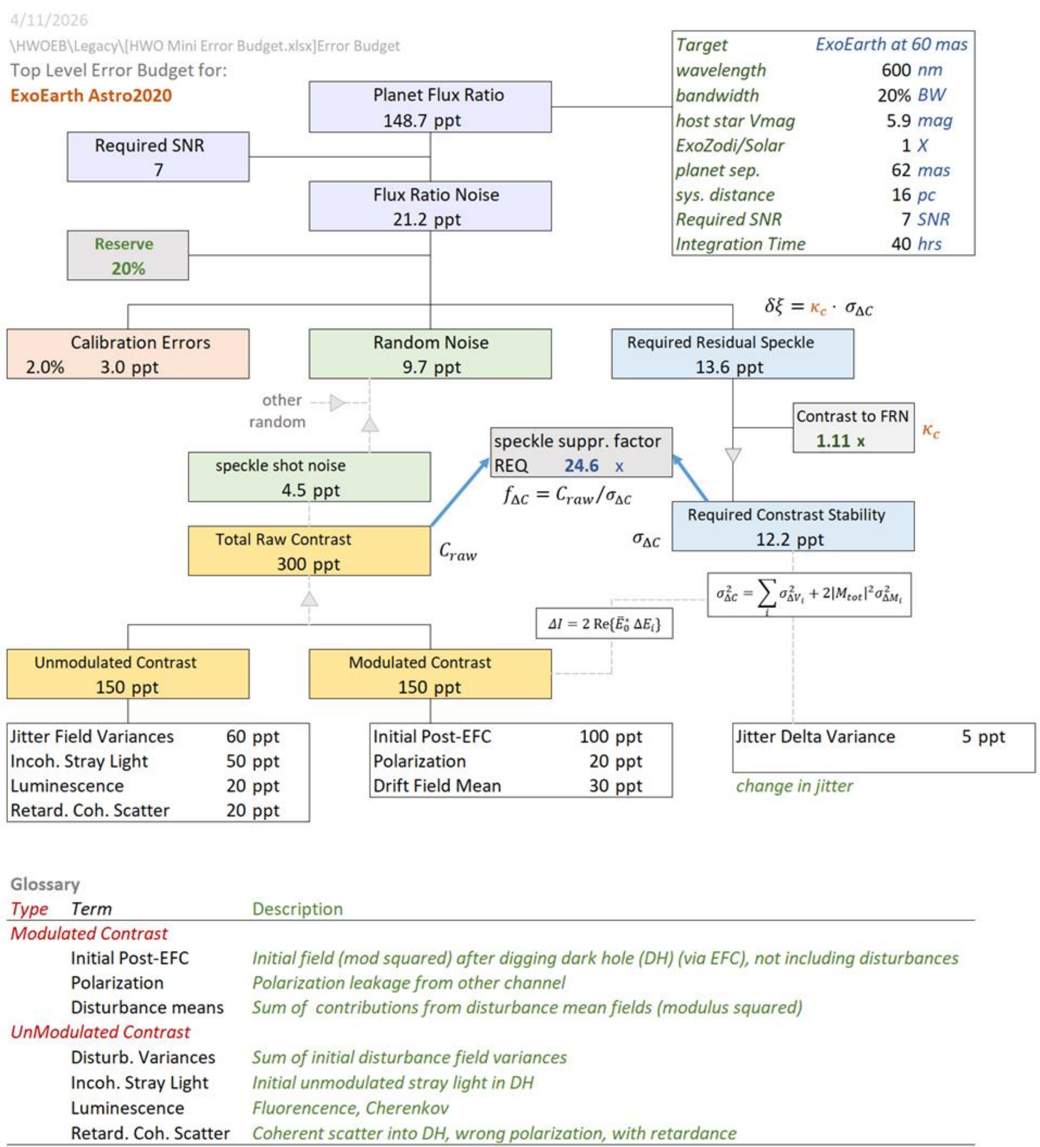

Fig 3: Scattered light error budget allocation flows from flux ratio to detect exoplanet with SNR = 7 and 40 hour integration time. Scattered light contributes to both the random noise branch of the FRN error budget via shot noise and to the residual speckle branch via the heterodyne mixing term.

Scattered light contributes to both the Random Noise and Residual Speckle branches of the FRN error budget. And scattered light can be both modulated (coherent) and unmodulated (incoherent). Modulated contrast is wavefront error that can be corrected via electric field conjugation (EFC) [21] and deformable mirror wavefront manipulation. The Unmodulated Contrast branch of the error budget cannot be corrected via deformable mirrors. Both are a flow down from the Total Raw Contrast allocation. To date, the best achieved contrast in testbeds has been at the level of ~ 4×10^{-10}, or 400 ppt. The error budget of Fig 3 assumes a slightly better total average raw contrast of 300 ppt.

3 Sources of Scattered Light

There are many sources of scattered light. As discussed in Appendix B, sources of scattered light include correlated surface structure (i.e. low- and mid-spatial frequency structure) and uncorrelated structure (microroughness and coating structure). Other sources of scattered light include contamination, micrometeoroid impacts, polarization leakage, ghost reflections, and edge diffraction. This assessment did not consider ghost reflections or edge diffraction.

3.1 Correlated Surface Structure

Correlated surface structure contributes to three terms in the FRN error budget: Initial Post-EFC, Drift Field Mean and Jitter Field Variance.

Initial Post-EFC speckle is caused by light scattered into the dark hole by static low- and mid-spatial structure of the residual wavefront error that is left unremoved after all wavefront control. Because this wavefront error has spatial structure, it produces speckle at specific angular locations in the dark hole. This analysis defines low-spatial structure to be structure whose spatial frequency scatters/diffracts energy directly into the dark hole. And mid-spatial structure is defined to be structure whose spatial frequency scatters/diffracts energy outside of the dark hole but contributes energy to the dark hole via a harmonic mixing process similar to the moiré effect. **[22]**

Drift Field Mean FRN, that is FRN caused by the drift of the mean field within an observation, is caused by slow wavefront drift – primarily caused by thermal transients. Jitter Field Variance FRN is caused by fast wavefront jitter – primarily caused by mechanical disturbances. Because exoplanet photons arrive at a rate of approximately 1 per minute, coronagraphy requires hours of integration time to get a dark hole image. As a result of this very long integration time, fast wavefront instability averages to a mean irradiance that can be subtracted by differential imaging, its noise contribution to the FRN error budget is via only speckle shot noise. But because slow wavefront instability cannot be subtracted, it contributes to both shot noise and residual speckle. The boundary between fast and slow depends on the science integration time (Fig 4). For a two-hour integration time, the boundary is 0.001 Hz. Any wavefront instability faster than a few Hertz contributes much less FRN than slow instability.

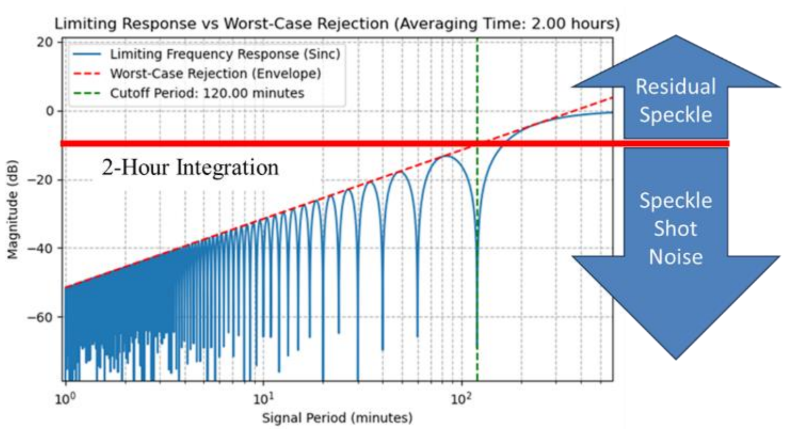

Fig 4: Because exoplanet photons arrive at approximately 1 per minute, coronagraphy requires hours of integration to create an image. Thus, because of integration averaging, fast wavefront instability (> 1 Hz) contributes significant less (<< 10X) flux ratio noise than slow wavefront stability (< 0.001 Hz). Fast instability contributes to speckle shot noise. Fast instability contributes to residual speckle noise.

3.1.1 Low-Spatial Frequency

This analysis defines low-spatial structure to be structure whose spatial frequency scatters/diffracts energy directly into the dark hole. To simplify deriving physical allocations of these error sources from the FRN error budget, this assessment uses Rayleigh-Rice (RR) Vector Scatter Theory (Appendix B.2.1) and assumes that all correlated structure produces a wavefront conjugate with the primary mirror. While the pupil plane simplification yields results consistent with other researchers, we acknowledge the caveat raised by the assessment's independent reviewers that it is insufficient to consider a system in which optical errors only occur at a pupil image, because chromatic Talbot effects lead to substantial chromaticity in the dark hole after EFC; and much of that is unresolved spatially or spectrally.

Using RR theory, the near-angle scatter throughput at a single angle is given by:

$$\tau_{NAS}(\theta) \equiv \frac{\Phi(\theta)_s}{\Phi_i} = \left(\frac{2\,\pi\,a}{\lambda}\right)^2 = \left(\frac{\pi\,w}{\lambda}\right)^2$$

Where a = peak-valley amplitude of the surface sinusoid and w = is amplitude of wavefront. Solving for w yields a first order estimate of the allowed residual WFE for 100 ppt of Initial Post-EFC, 30 ppt of Drift Field Mean and 60 ppt of Jitter Field Variance Contrast (**Table 1**).

Initial Post-EFC: $w = \left(\frac{\lambda}{\pi}\right)\sqrt{100\;ppt}$

Drift Field Mean: $w = \left(\frac{\lambda}{\pi}\right)\sqrt{2\;x\;30\;ppt}$

Jitter Field Variance: $w = \left(\frac{\lambda}{\pi}\right)\sqrt{30\;x\;60\;ppt}$

The factor of two for Drift Field Mean is because the total peak-to-valley drift is twice the mean. The factor of 30 for Jitter Field Variance is because, as shown in **Fig. 4**, the high-speed WFE or jitter averages to a mean value that can be subtracted. It is the variance or uncertainty of this mean value that contributes to the FRN error budget. Variance is equal to the uncertainty of estimating the mean's true value or its standard deviation divided by square root of sample number:

$$\text{Uncertainty of Mean Estimate of a Sine Wave} = \sigma/\sqrt{N} = PV/\sqrt{8N}$$

Given that the photon arrival rate is about 1 per minute, a 2-hour integration has N = ~ 120 photons; and $\sqrt{8\ x\ 120} = \sim 30$.

Table 1: WFE Specification as a function of Wavelength

FRN Error Budget Term	Wavelength			
	300 nm	500 nm	600 nm	1800 nm
Initial Post-EFC STATIC WFE [PV]	1.0 pm	1.6 pm	2.0 pm	5.8 pm
Drift Field Mean WFE [PV]	0.7 pm	1.2 pm	1.5 pm	4.4 pm
Jitter Field Variance WFE [PV]	4 pm	7 pm	8 pm	25 pm

Again, Table 1 gives the PV amplitude of a correlated sinusoidal wavefront error that produces a speckle at a specific location in the dark hole. A different sinusoid spatial frequency of the same amplitude will produce a speckle with the same contrast at a different location in the dark hole. Finally, these results are completely consistent with multiple prior studies which derived specifications based on diffraction theory and wavefront propagation. **[12-16]**

3.1.2 Mid-Spatial Frequency

This analysis defines mid-spatial structure to be structure whose spatial frequency scatters/diffracts energy outside of the dark hole but contributes energy to the dark hole via a harmonic mixing process. **[22, 23]** **Figure 5** illustrates a simple case for a wavefront with two cosine errors of different spatial frequencies (whose direct scatter would be beyond the dark hole outer working angle) of PV amplitudes A1 and A2. Mathematically, via a Taylor series expansion, these two electric fields produce a sub-harmonic field with a spatial frequency equal to the difference between their individual frequency and an amplitude equal to their average.

$$A = \frac{A_1 A_2}{2}$$

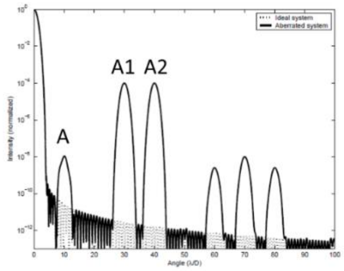

Fig 5: Two electric fields with different spatial frequencies outside of the dark hole with PV amplitudes of A1 and A2 'mix' to produce a single electric field of amplitude A equal to the average of the two and a spatial frequency equal to the difference between the two. [22]

Because EFC (Electric Field Conjugation) can compensate for static 'folded' electric fields, the previously defined Initial Post-EFC PV static WFE specification is unchanged: it does not matter if residual error is from Low-Spatial or Mid-Spatial Folding. But EFC cannot compensate for dynamic 'folded' electric field. Thus, the specifications for Drift Mean and Jitter Field Variance must include mid-spatial frequency errors. Because the folded amplitude in the dark hole is A/2, it takes twice as much mid-spatial instability amplitude to produce the same speckle noise as low-spatial instability amplitude. Extending the analysis to mid-spatial, this assessment arbitrarily allocated FRN error budget between low- and mid-spatial frequency to give each the same WFE amplitude (**Table 2**).

$$\text{Drift Field Mean Low-Spatial: } w = \left(\frac{\lambda}{\pi}\right)\sqrt{2\ x\ 24\ ppt}$$

$$\text{Drift Field Mean Mid-Spatial: } w = \left(\frac{\lambda}{\pi}\right)\sqrt{2\ x\ 6\ ppt}$$

$$\text{Jitter Field Variance Low-Spatial: } w = \left(\frac{\lambda}{\pi}\right)\sqrt{30\ x\ 48\ ppt}$$

$$\text{Jitter Field Variance Mid-Spatial: } w = \left(\frac{\lambda}{\pi}\right)\sqrt{30\ x\ 12\ ppt}$$

Table 2: WFE Specification as a function of Wavelength

FRN Error Budget Term	Wavelength			
	300 nm	500 nm	600 nm	1800 nm
Initial Post-EFC STATIC WFE [PV]	1.0 pm	1.6 pm	2.0 pm	5.8 pm
Drift Field Mean Low-Spatial WFE [PV]	0.65 pm	1.1 pm	1.3 pm	4.0 pm
Drift Field Mean Mid-Spatial WFE [PV]	0.65 pm	1.1 pm	1.3 pm	4.0 pm

Jitter Field Variance Low-Spatial WFE [PV]	3.6 pm	6 pm	7.2 pm	21.7 pm
Jitter Field Variance Mid-Spatial WFE [PV]	3.6 pm	6 pm	7.2 pm	21.7 pm

Again, please remember these are single frequency amplitudes that produce speckle noise at a specific dark hole location.

3.2 Uncorrelated Surface Structure

While correlated surface structure places energy into specific angular locations in the dark hole (as a function of correlated spatial structure), uncorrelated surface structure scatters light in all directions, (**Fig. 6**) producing a diffuse 'haze' over the dark hole. Typically, one considers diffuse scatter to be incoherent. But in this case, it is at least partially coherent because the optical surfaces are very smooth (<< λ) and Coronagraphs operate on narrow spectral bands of up to 20%. Therefore, the coherence length of the spectral band is longer than the optical surface roughness. Light scattered from a single point will have 'zero' optical path difference (OPD) from the input wavefront that illuminates that scattering point. And as the host star's wavefront propagates through the optical system, each time it reflects off an optical surface, a small amount becomes a diffuse E-Field, scattered by uncorrelated microstructure, that is in-phase (coherent) with the wavefront. This scattered E-Field both contributes to the heterodyne mixing term of Eq. 1 that produces speckle noise and introduces a DC-bias to the dark hole.

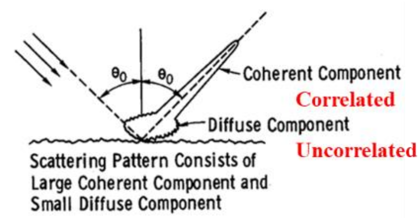

Fig 6: Uncorrelated surface structure scatters light diffusely into all angles. **[24]**

Because it remains unclear whether this diffuse scatter can be modulated via EFC, this assessment conservatively places scattered light from uncorrelated structure in the un-modulated FRN error budget branch. Table 3 proposes a potential sub-allocation of the 50 ppt Straylight FRN allocation.

Table 3: Sub-Allocation of 50 ppt Straylight FRN Allocation	
Total Straylight	50 ppt
• Reserve	15 ppt
• Surface Microstructure	20 ppt
• Coating Structure	7.5 ppt
• Contamination	5 ppt
• Micrometeoroid Impacts	2.5 ppt

3.2.1 Surface Microstructure

As discussed in Appendix B, from Generalized Harvey-Shack Scalar Scatter Theory and PSD theory, diffuse scatter amplitude is determined by surface microstructure RMS amplitude (σ) and correlation length (ℓ).

$$PSD_0 = \pi \ell^2 \sigma^2 \qquad \text{[Eq 2]}$$

Surface structure beyond the PSD correlation length is correlated and produces angular scatter at specific angles into the dark hole. Surface structure below the correlation length is uncorrelated and produces diffuse scatter across the entire dark hole. The PSD(0) value is linearly proportional to the diffuse scatter power per solid angle. **Figure 7** (right side) illustrates that PSD(0) depends on both RMS amplitude and correlation length. Having just a smooth RMS (long correlation length) does not guarantee a small PSD(0) or small diffuse scatter amplitude. **[25]**

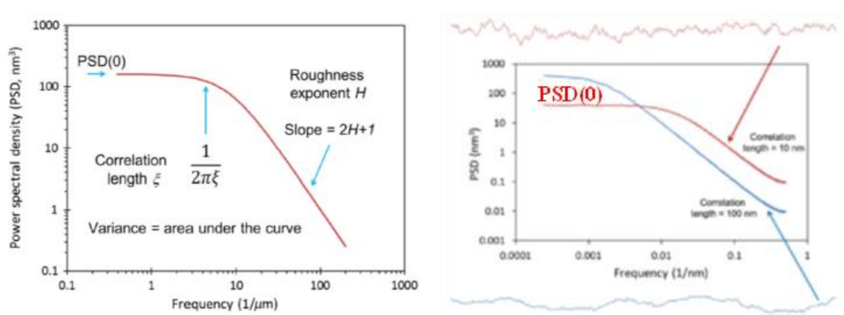

Fig 7. Correlated Structure scatters light into specific angles. Uncorrelated Structure scatters light diffusely into all angles. PSD Correlation Length defines boundary between correlated and uncorrelated surface structure. **[25]**

And as discussed in Appendix B.3, near-angle scatter throughput is proportional to a mirror's BRDF:

$$\tau_{NAS} \equiv \frac{\Phi_s}{\Phi_i} = BRDF\ d\Omega = BRDF \cdot \pi \left(\frac{\lambda}{D}\right)^2$$

Solving for BRDF

$$\mathrm{BRDF} = \tau_{NAS} \frac{1}{\pi}\left(\frac{D}{\lambda}\right)^2 \qquad \text{[Eq 3]}$$

Combining Eq 1 and 2 and using the relationship between PSD and BRDF from Appendix B.3 for smooth mirrors at near normal incidence gives:

$$\mathrm{PSD}[\text{Å}^2\ \mu\mathrm{m}^2] = \left[\frac{10^8\ \lambda^4}{16\pi^2}\right] \cdot \mathrm{BRDF} \qquad \text{[Eq 4]}$$

Where 10^8 converts units from μm^4 to $Å^2\ \mu m^2$.

Now, using the relationship between surface statistics and PSD (Eq 2), between BRDF and Throughput (Eq 3), between BRDF and PSD (Eq 4) and assuming Gaussian surface statistics, a general expression can be derived that specifies an optical surface's statistics to meet a given near-angle scatter throughput error budget allocation:

$$\ell^2\,\sigma^2 = \frac{PSD}{\pi} = \left[\frac{10^8\ \lambda^4}{16\pi^3}\right] \cdot \mathrm{BRDF} = \left[\frac{10^8\ \lambda^4}{16\pi^3}\right] \cdot \tau_{NAS}\,\frac{1}{\pi}\left(\frac{D}{\lambda}\right)^2 = \left[\frac{10^8\ D^2\lambda^2}{16\pi^4}\right] \cdot \tau_{NAS}$$

$$\sigma\,\ell\ [\text{Å}\ \mu\mathrm{m}] < 10^4\,\frac{\lambda D}{4\pi^2}\sqrt{\tau_{NAS}}$$

In Section 3.1, to simplify the correlated structure analysis, it was assumed that all scatter came from a wavefront conjugate with the primary mirror. To simplify the uncorrelated structure, we assume that all surfaces have the same statistics and contribute equally to the total FRN error budget diffuse scatter allocation. As a reminder, per Appendix B, diffuse scatter from optical surfaces sums (**Fig B-3**). Assuming an allocation of 20 ppt for diffuse scatter (Table 3) and that there are approximately 20 optical surfaces before the coronagraph focal plane mask (**Fig 8**), the simplified analysis allocates 1 ppt of diffuse scatter per optical surface.

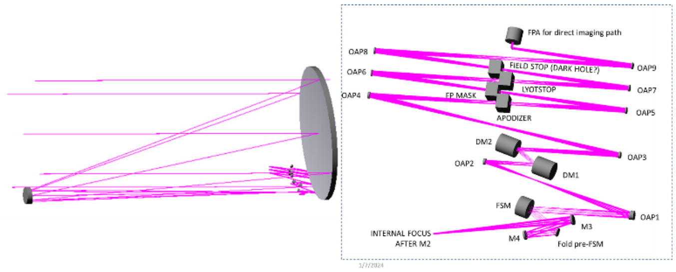

Fig 8. Every optical surface before the coronagraph focal plane mask is fully illuminated by host star light and can contribute scattered light into the dark hole.

Assuming a 6-m telescope, Table 4 gives the allowed microstructure roughness, σ, (in Å) as a function of wavelength, λ, and microstructure correlation length, ℓ, (both in μm) for a single surface to meet a 1 ppt near-angle scatter throughput, τ_{NAS}, specification.

Table 4: Surface RMS Microstructure [Å] to have NAS Throughput < 1 ppt				
	Wavelength (λ) [μm]			
Correlation Length (ℓ) [μm]	0.300	0.680	1.000	1.800
10	450	1020	1500	2700
100	45	102	150	270
1,000	4.5	7.5	15	27
10,000	0.5	0.8	1.5	2.7

While the above simplified analysis is illustrative, as will be explained in Section 4, it is not very informative. Optical surfaces do not contribute equally to diffuse scatter in the dark hole.

3.2.2 Coating Microstructure

In addition to scatter from surface microstructure, Dr. Breckinridge was concerned about scatter from the reflecting coating. Aluminum reflectance coatings have aluminum grain structure (sometimes called columnar structure) that results from the physical vapor deposition process. [26] Consistent with the analysis of Section 3.2.1, the GSFC Coating Team developed a measurement and analysis process to quantify the PSD and statistics (σ, ℓ) of polished ULE® and

ZERODUR® low-expansion glass substrates before and after applying two candidate HWO coatings [27-29]:

- Al+XeLiF: 65 nm Al + XeF_2+ 15 nm LiF
- Al+XeMgF_2: 65 nm Al + XeF_2+ 21 nm MgF_2

The surfaces were measured over different fields of view via different magnifications. (Fig 9) Both coatings increased surface roughness from 3 to 4 Å rms to close to 10 Å rms at the highest resolution measurement. The larger field-of-view measurements underestimate the surface roughness because at that magnification the instrument's spatial resolution is too coarse, i.e. filters out (averaging over) the high frequency parts of the roughness spectrum. **[27-29]**

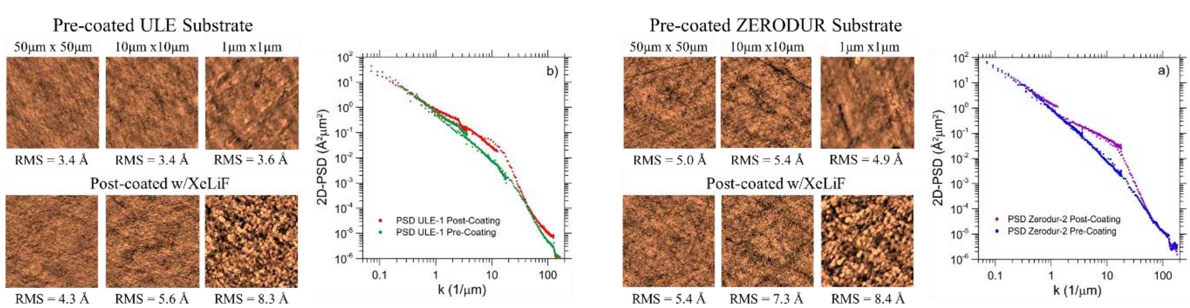

Fig 9. ULE and Zerodur surfaces were measured at different magnifications before and after coating. In all cases, coating increased surface roughness.

Band limited PSDs were calculated for each measurement and combined into a 2D PSD for the surface. (see Appendix B.3.3) The PSDs of the 'pre-coating' surfaces exhibited a nominal fractal surface. The 'coated' surfaces had a more complicated structure. Analysis revealed that the coated surfaces were composed of multiple band-limited PSDs. (Fig. 10) Because of the columnar structure of the coating, the coating's greatest impact occurs at the shortest correlation lengths. The coating has only a minor impact on PSDs with longer correlation lengths (i.e. yellow curve) which is likely associated with surface microstructure. **[27-29]**

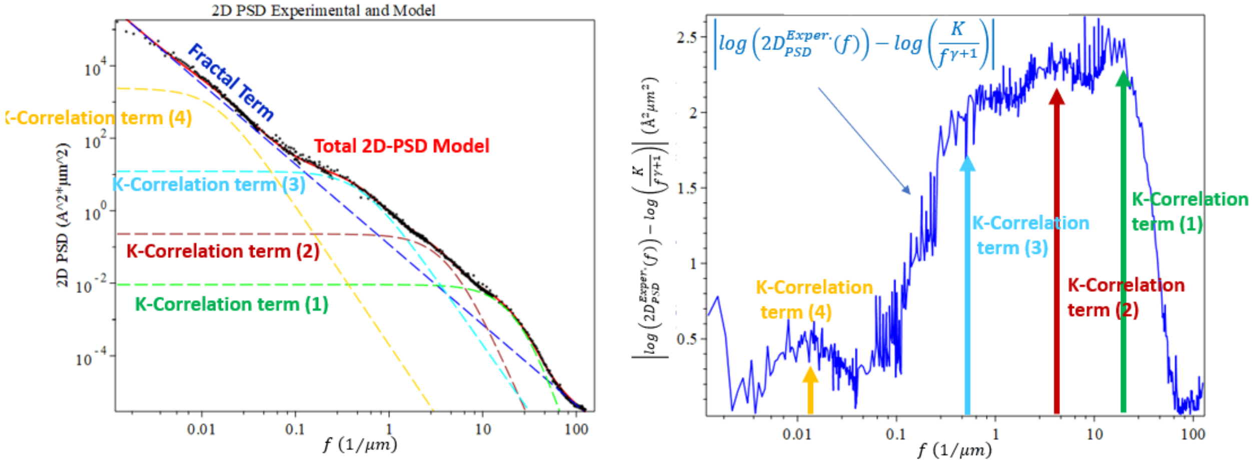

Fig 10. Each magnification yields a Band-Limited PSDs which was combined into a Total 2D PSD model.

Based on the analysis shown in Fig 10, for the modeling of Section 4, four arbitrary statistical surface PSDs were defined, each with a surface roughness of 10 Å rms but with different correlation lengths:

- PSD #1: 0.1 µm Correlation Length (between red and green arrows)
- PSD #2: 1 µm Correlation Length (approx. blue arrow)
- PSD #3: 10 µm Correlation Length
- PSD #4: 100 µm Correlation Length (approx. yellow arrow)

Per the analysis of Section 3.2.1, PSD #1 will not be a significant source of diffuse straylight contrast because its correlation length is too short. But PSD #4, which is mostly associated with native surface microstructure, is a significant source of diffuse scatter.

3.3 Surface Contamination

Surface contamination is not caused by correlated surface structure. It is caused by single scatters. Its scatter is a combination of diffuse and directional based on the particle's size and shape. And because it may or may not modulate, this assessment conservatively assigned it to the FRN unmodulated contrast scattered light allocation branch. While contamination particles are not typically spherical, particulate contamination is generally modeled via Mie scatter. Mie scatter is directional and the larger the particle the narrower and more directional its scatter cone (**Fig. 11**). Also, while we did not consider polarization as part of the contamination analysis, it is proper to note that each polarization state has its own scatter profile.

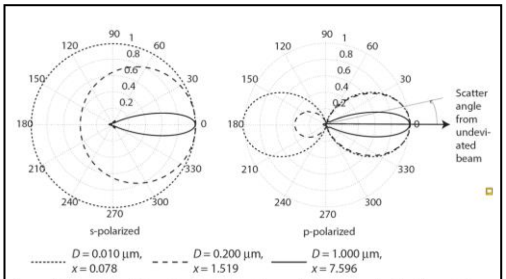

Fig. 11 Normalized intensity vs scatter angle for s-polarization (left) and p-polarization (right). D is sphere diameter. [30]

Identical to primary mirror microstructure, a scattering particle on the primary mirror of a telescope/coronagraph will produce a spherical wavefront that is focused (by the secondary and aft-optics) into the conjugate pupil. The coronagraph collimates this focus such that most of its light passes the focal plane mask unobscured and is reimaged into the dark hole as a collimated E-field. Because the particle is located on the PM, its E-Field is coherent and in phase with the host star's light – thus, it increases the heterodyne amplification of any wavefront instability (Eq 1). Similarly, a particle on the secondary mirror produces a spherical E-field in the dark hole that adds with the primary mirror E-field and E-fields from all other surfaces. Given the 5 ppt FRN allocation for contamination scatter (Table 3) and that there are approximately 20 optical surfaces before the coronagraph focal plane mask (**Fig 8**), a simplified analysis allocates 0.25 ppt of contamination per optical surface.

All surfaces have contamination, but because each contamination population is unique it is impossible to deterministically model contamination scatter. Thus, contamination is described statistically via Cleanliness Level (CL) and BRDF. [31] CL corresponds to the average particle size per 0.1-m^2. (**Fig 12**) Thus, a CL-200 Surface has average of one 'equivalent' 200-µm particle per 0.1-m^2.

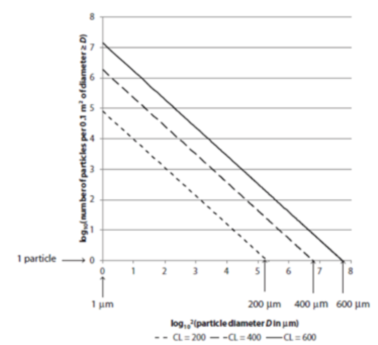

Fig. 12 Number of particles of Diameter larger than D per CL [30]

BRDF varies with particle diameter to the 4th power (**Fig 13**). Consequently, large particles contribute more scatter throughput than small particles. But standard cleaning processes can typically remove particles larger than 50 µm. [32] Also, **Fig 13** illustrates how small amplitude surface microstructure creates a near-angle BRDF floor.

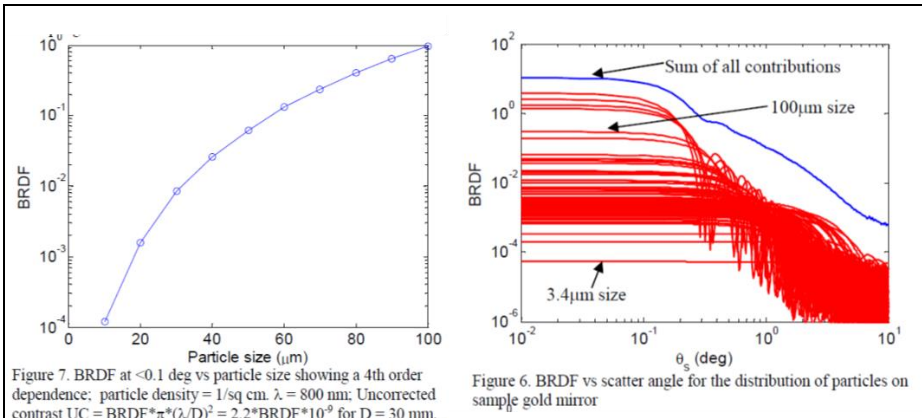

Fig.13 Larger particles produce more scatter and larger BRDF [32]

Peak BRDF values can be derived for each cleanliness level. [30, 31] Thus, using the BRDF to NAS throughput equation, a surface contamination specification can be defined for a given per surface scatter allocation. For a 6-m telescope and a 0.25 ppt per surface allocation, the peak BRDF is:

$$\text{BRDF}_0 = \frac{\tau_{NAS}}{\Omega_{\text{core}}} = \frac{0.25 \cdot 10^{-12}}{\pi \cdot 10^{-14}} \simeq 8 \ [1/\text{sr}]$$

From **Fig 14**, a peak BRDF of 8 corresponds to a cleanliness level of ~ CL-400 for a wavelength of 633 nm. For comparison, Webb had a CL-600 specification. It is important to note that the surfaces will need to be cleaner if the coronagraph operates at shorter wavelengths – because particles scatter more at shorter wavelengths. Furthermore, it is not necessary to divide the contamination scatter allocation equally between surfaces. Because scatter sums, one could allocate more contamination to the telescope mirrors and require the coronagraph mirrors to be cleaner.

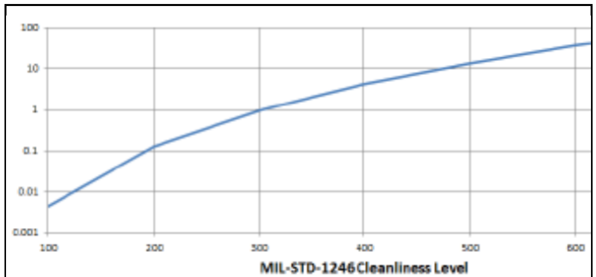

Fig.14 Peak BRDF (at λ = 633 nm) vs CL [31]

4 FRED® Straylight Analysis of HWO EAC-1

To move beyond simple first order approximations, Photon Engineering created a straylight model of HWO EAC-1 in FRED® (**Fig. 15**). The model was used to investigate the near-angle scatter into the coronagraph dark hole caused by correlated surface structure, uncorrelated surface/coating microstructure, contamination and polarization leakage. Modeling was performed by assigning PSDs and Cleanliness Levels (CL) to each optical surface. Rays were propagated through the system to the dark hole where they were converted into a BSDF distribution. Per Appendix B.3, BSDF is converted into near-angle scatter throughput and used to assess specifications consistent with potential FRN error budget allocations.

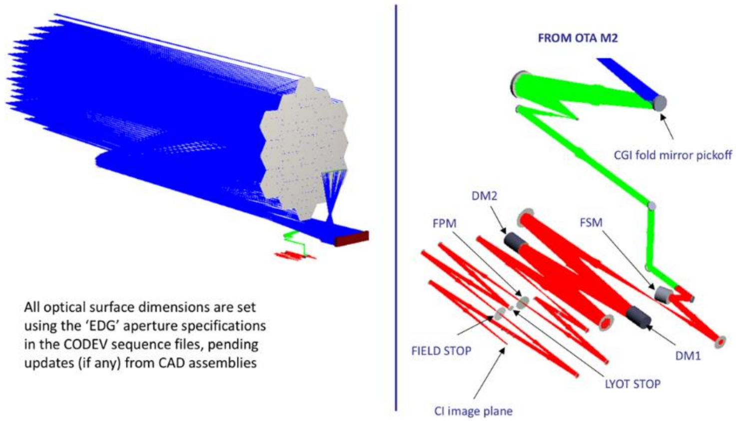

Fig 15. FRED® Model of HWO EAC-1

Multiple cases were analyzed. Of these, we report on three:

- Case 1: JPL PSD + PCL 300 (all surfaces)
- Case 2: Coating PSD #3 ($\sigma = 10$ Å rms, $\ell = 10$ µm) + CL-300/150/75
- Case 3: Coating PSD #4 ($\sigma = 10$ Å rms, $\ell = 100$ µm) + CL-300/150/75

Case 1 used a set of PSDs for each optical surface supplied by JPL. (**Fig. 16 left**) [33] (JPL uses these PSD in their diffraction modeling) and assumed a particulate cleanliness level (CL) of 300 for all surfaces. Case 2 and Case 3 assigned variations of PSDs found from the Coating Structure analysis to every surface in the EAC-1 model. For each Case, FRED® modeled the scattered light in the dark hole before EFC correction and the contribution of each surface to this dark hole light.

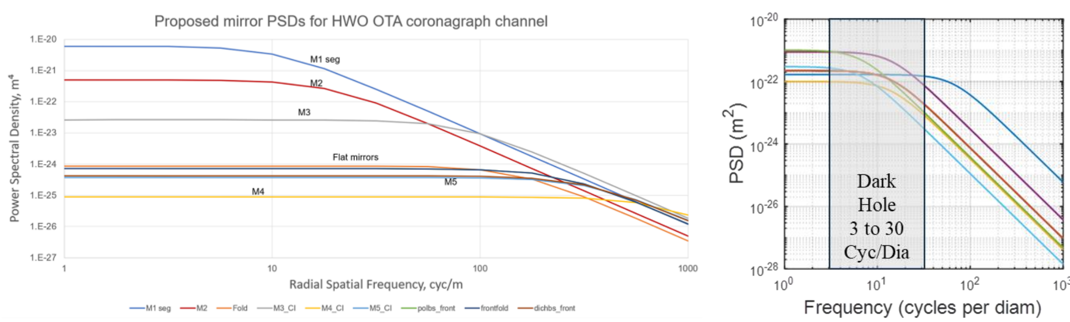

Fig 16. (left) JPL provided PSDs for HWO EAC-1 Surfaces; **(right)** JPL PSDs rescaled to dark hole.

4.1 Case 1: JPL PSD + PCL 300 (all surfaces)

The JPL PSDs are composed of correlated structure with cycles ranging from approx. 5 to 1000 cycles per diameter. (**Fig 16 right**) Each structure spatial frequency scatters energy into a specific angle. Because the JPL PSDs have a power law amplitude falloff at spatial frequencies that angularly scatter light directly into the dark hole, FRED® predicts that EAC-1 will have scattered light in the dark hole with a power law falloff (**Fig 17 left**). And, because Case 1 uses the same PSDs as JPL's diffraction propagation codes, FRED®'s angular scatter distribution is similar to those code's pre-EFC correction contrast predictions (**Fig 17 right**). [34, 35]

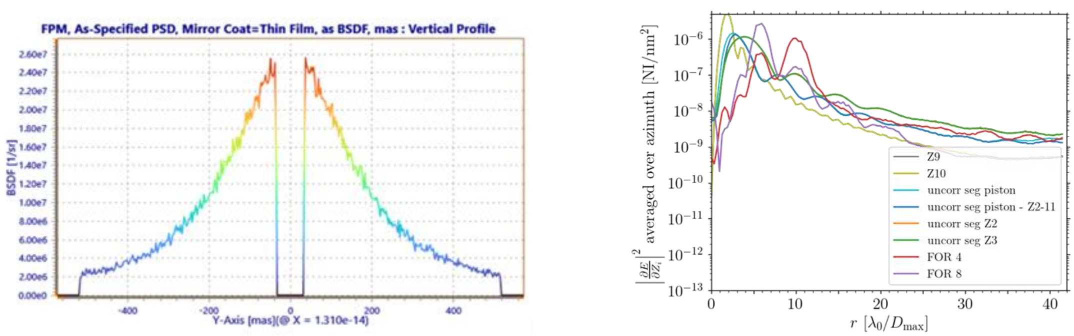

Fig 17. (left) FRED® predicted dark hole BRDF; **(right)** JPL predicted dark hole pre-correction contrast. [35]

FRED® predicts that the max contrast at the dark hole inner working angle (IWA) is ~ 250,000 ppt (which is a very large number). But, because this angular scatter is caused by correlated structure, it can be corrected by EFC WFSC.

It is interesting to note that while JPL assigns the highest PSD value to the primary mirror, FRED® finds that for the JPL PSDs the secondary mirror (M2), tertiary mirror (M3) and polarizing beam splitter all contribute more scatter to dark hole than the primary mirror (M1). (**Fig 18**) Smaller surfaces and surfaces closer to the focal plane mask contribute the most scattered light.

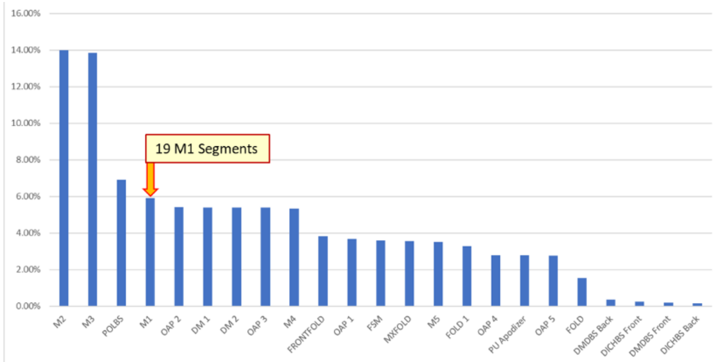

Fig 18. FRED® predicted per surface scattered light contribution to dark hole. Secondary mirror (M2), tertiary mirror (M3) and polarizing beam splitter all contribute more scatter to dark hole than the primary mirror (M3).

4.2 Case 2 and Case 3

Because FRED® operates on PSDs, it can model the diffuse scattered light contributed to the dark hole by uncorrelated micro-structure (Cases 2 and 3). Because the correlation length of these PSDs is short, there is no correlated angular scatter into the dark hole. All scatter from the Case 2 and Case 3 PSDs is diffuse. As expected, FRED® predicts a uniform contrast in the dark hole (**Fig 19 left**). It is important to note that it is the smallest surfaces, and the surfaces closest to the focal plane mask that contribute the most diffuse scatter from microstructure (**Fig 19 right**). But, this is a bit misleading because Cases 2 and 3 arbitrarily assign the same PSD to every surface in the EAC-1 model.

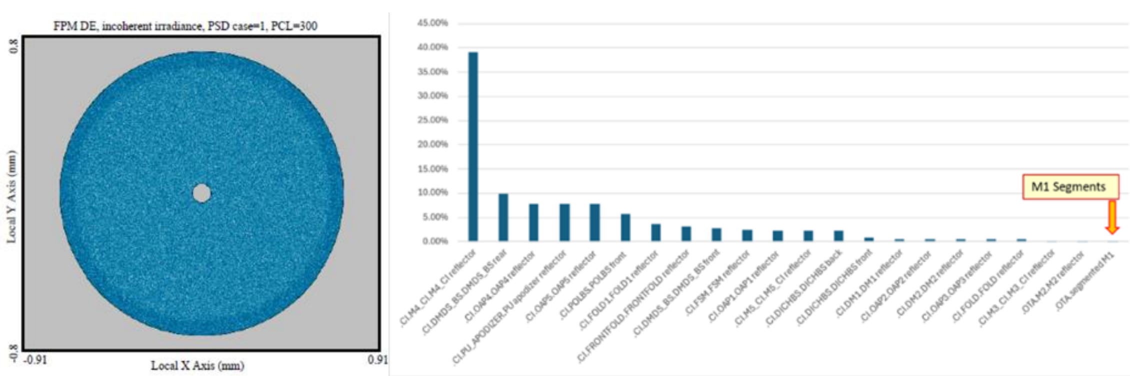

Fig 19. (left) Uncorrelated Surface Microstructure produces uniform Diffuse Scatter in the Dark Hole. **(right)** The smallest surfaces and surfaces closest to the Focal Plane Mask contribute the most diffuse scatter into the Dark Hole.

Table 5 summarized the diffuse scatter introduced into the dark hole for the Case 2 and Case 3 correlation lengths and contamination levels. For Case 2, because the correlation length of the surface is small, surface contamination is a larger contributor to dark hole diffuse scatter contrast than surface microstructure. For Case 3, because the correlation length is longer, surface contamination is less of a contributor.

Table 5: Diffuse Scatter Contrast as a function of Correlation Length and Contamination			
Case 2: Diffuse Scatter for 10 Å rms surface with 10 µm correlation length vs Contamination Level			
Cleanliness Level	Irradiance [W/mm^2]	BSDF [1/sr]	Scatter Contrast [ppt]
75	2.3E-8	~ 2 E3	20
150	7.6E-8	~ 6 E3	60
300	1.9E-6	~ 1.6 E5	1600
Case 3: Diffuse Scatter for 10 Å rms surface with 100 µm correlation length vs Contamination Level			
Cleanliness Level	Irradiance [W/mm^2]	BSDF [1/sr]	Scatter Contrast [ppt]
75	2.0E-6	~ 2 E5	2000
150	2.3E-6	~ 2 E5	2000
300	3.6E-6	~ 3 E5	3000

The fundamental unresolved question is whether diffuse scatter is physically modulable. If unmodulable, to meet the contrast error budget allocation will require coronagraph surfaces with:

- 10 Å RMS, < 10 µm correlation length and CL-75, or
- 5 Å RMS, 10 µm correlation length and CL-150, or
- 1 Å RMS, 100 µm correlation length and CL-75

Fortunately, as indicated in **Fig 18**, not every surface needs the same specification. Each surface contributes scatter differently depending upon its solid angle to the dark hole. The smallest surfaces and surfaces closest to the focal plane mask contribute the most. Figure 20 shows an example of a 'distributed' contamination allocation published by Balasubramaniam, Shaklan and Give'on (2009). **[35]**

Optic Dia (m)	Typical # of optics in system	Contrast budget per optic for 25% BW	CL requirement on each optic	PAC requirement on each optic	CL requirement with 4x margin due to model assumptions	PAC requirement with 4x margin due to model assumptions
0.03	5	$6x10^{-12}$	<75	<0.00009	<50	<0.00002
0.1	5	$6x10^{-12}$	<150	<0.001	<100	<0.0002
1.0	2	$1.5x10^{-11}$	<400	<0.09	<300	<0.02
4.0	1	$1x10^{-11}$	<700	<1.5	<500	<0.25

Fig 20. From REF 35, per surface contamination allocation that distributes 37 ppt of contrast [36]

4.2.1 Can Diffuse Scatter be Modulated?

Regarding the question of modulated or unmodulated, per the assessment's independent reviewers, light with coherence that cannot be resolved is light that appears unmodulated. If the source of the scatter cannot be decomposed into spatially correlated terms that correspond to specific locations within the dark hole, the DM will have to resort to a complex mixture of "hard" modes. To test these constraints, a simulation was conducted using an existing propagation code model of the HWO testbed which contains a few OAPs in relays prior to the focal plane mask (in this case, a vortex). Without any aberrations, the contrast was $<10^{-11}$ over a 10% bandpass and over an annular Airy Disc ring from 3 to 9 λ/D. The geometric beam size was 300 pixels across. Adding to each (otherwise unaberrated) optic a pixel-to-pixel phase noise with a Gaussian distribution of RMS = 500 pm, the contrast degrades to $4x10^{-9}$. Running EFC returns the contrast to <1e-11 contrast. The main caveat is that the optics in the testbed are all close to pupils, so there aren't strong chromatic amplitude errors being generated by them. There may be increased limits on optics far from pupils or near foci, where the beam diameter changes with wavelength and phase errors can generate chromatic amplitude errors (such a case is much harder to simulate accurately). [37] This simulation implies that EFC may be able to correct diffuse scatter caused by surface roughness, but the result is not definitive. Therefore, this assessment chose to keep diffuse scatter in the unmodulated contrast branch of the FRN error budget.

Additionally, Balasubramaniam, Shaklan and Give'on (2009) report that EFC correction for contamination is limited by the absorption of the particle. (**Fig 21**) The amount of contrast that can be corrected roughly equals the uncorrected contrast scaled by the average particle reflectance. Thus, a shiny 'reflective' particle produces more uncorrected contrast than a black 'absorbing' particle. For typical dust, the unmodulated correction limit is ~ 40% of the raw contrast. **[36]**

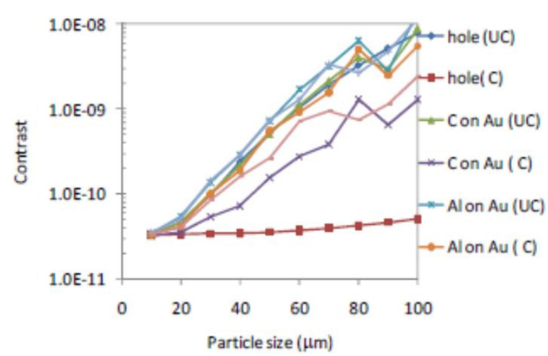

Fig. 21 Uncorrected (UC) and corrected contrast © with various particle types. One particle is placed on a 30 mm pupil of the Apodizer Pupil Coronagraph in this broadband simulation with EFC. Where Hole = an ideal black hole, C = a carbonaceous black particle, and Al = a metallic shiny particle. **[36]**

4.2.2 Test Bed Unmodulated Contrast Noise Floor

As mentioned in Section 1, no coronagraph testbed has yet achieved its theoretical performance limit. Theoretically EFC and DMs should be able to 'dig' an arbitrarily deep Dark Hole - limited only by temporal wavefront instability and DM resolution. But, even with static wavefronts, test beds have been unable to achieve theoretical performance. Test beds reach a noise floor that cannot be modulated by DMs and contribute shot noise into the FRN error budget.

- HCIT (High Contrast Imaging Testbed) had 10,000 ppt of unmodulated contrast "which is independent of the errors we injected." (2020) **[3]**
- DST (Decadal Survey Testbed) had 200 ppt of unmodulated contrast of which the source of 50 ppt was unknown. The rest was attributed to jitter and ghost reflections. (2019) **[4]**
- Roman OMC (Occulting Mask Coronagraph) Testbed had 3,000 to 4,400 ppt (depending on jitter amplitude) of unmodulated contract (2017) **[5]**

While causality of the testbed unmodulated contrast noise floor is not fully understood, the predicted diffuse scatter values in Table 5 are consistent with the reported testbed values.

5 Micrometeoroid Impacts

Similar to contamination, micrometeoroid impacts produce scatter that can reach the dark hole. But there are differences. One difference is that micrometeoroids are likely to only impact the primary mirror. Another is that micrometeoroid impacts are significantly larger and more complex than contamination. (**Fig 22**) Typical impact morphology consists of a small deep central hole, several 10s to several 100s of micrometers wide, surrounded by an impact pit ~50X larger, surrounded by a spall region ~11X larger than the pit diameter and ~10X larger than its depth. **[38]**

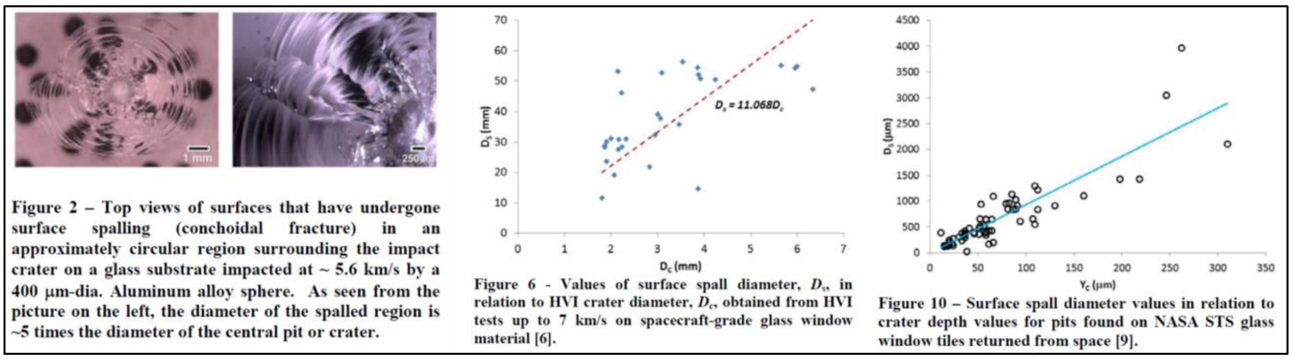

Fig 22. Figures from REF 38 showing that micrometeoroid impacts produce a central pit surrounded by spall (fracture zone). On average the spall is ~11X larger than the pit diameter and ~10X larger than the pit depth. **[38]**

The size of the impact pit and spall diameter are a function of the kinetic energy of the impact – not the size of the impacting particle. **Fig 23** shows that for the highest energy impacts, the spall diameter is in the 1 to 100 mm range. Therefore, a micrometeoroid impact's scatter may be significant and narrow. Finally, there is no accepted method for modeling scatter from micrometeoroid impacts.

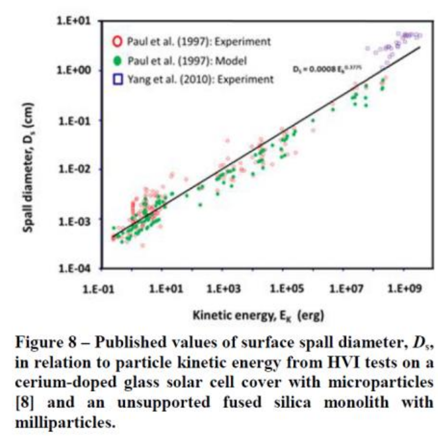

Fig. 23 Figure from REF 38 showing that spall diameter is larger for higher kinetic energy impacts. **[38]**

One approach may be cleanliness level. Because CL corresponds to the particle size whose average density is one particle per 0.1-m^2 surface area, one can calculate a CL for a single micrometeoroid impact of a given size on the primary mirror by its area. If the contrast allocation for micrometeoroid impacts is 2.5 ppt (Table 3), then the primary mirror needs a peak BRDF of less than 80 which corresponds to a CL-600 (one 600 μm diameter particle per 0.1-m2). (**Fig 14**) For a 28-m^2 area primary mirror this is equal to a single 168-mm diameter impact.

Another approach may be to model the impact as a circular hole surrounded by a conical or Gaussian shape pit that both diffract, surrounded by a spall region that scatters Lambertian. Starting with the hole, using 2D Gaskill notation **[39]**, if one assumes that the micrometeoroid impact pit is a cylindrical circle of diameter d, then its scattered light will have a 'Sombrero' amplitude profile and its scattered light amplitude at small angles is approximately d^2 times the ratio of power onto hole vs onto the primary mirror.

$$\mathrm{cyl}(r/d)\ \langle\mathcal{F}\rangle\ d^2 \cdot \mathrm{somb}(d\,\rho) = \sim d^2 \text{ for small angles}$$

$$\tau_{NAS} = \sim \frac{d^4}{D^2}$$

It is the same for the scattered light amplitude at small angles from a Gaussian (or conical) pit:

$$\mathrm{Gaus}(r/d)\ \langle\mathcal{F}\rangle\ d^2 \cdot \mathrm{Gaus}(d\,\rho) = \sim d^2 \text{ for small angles}$$

Figure 24 shows the contrast produced by holes or pits as a function of diameter. A hole of 3.1-mm diameter produces the error budget allocated 2.5 ppt of contrast. Impacts with a hole smaller than 1-mm contribute negligible scatter to the dark hole. But pit diameters have the potential of contributing significant contrast.

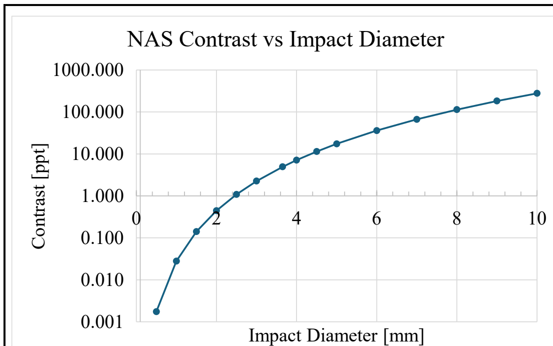

Fig. 24 Contrast vs impact hole diameter

Now, considering the spall region. If it scatters as a Lambertian surface, its BRDF is (1/π) and a spall region of diameter d will have a near-angle-scatter throughput of:

$$\tau_{NAS} = \left(\frac{d^2}{D^2}\right) \cdot BRDF \cdot \Omega_{Core} = \left(\frac{\lambda d}{D^2}\right)^2$$

Assuming that the spall is 44 mm, i.e. 11X larger than the hole, then the contrast for a 6-m primary mirror and λ = 633 nm is 0.6E-6 ppt. Further study is needed to determine if the Lambertian assumption is valid. One potential method to test this assumption is to quantify the total integrated scatter of micrometeoroid impacts (see Appendix B.5).

This study does not make an assessment as to the extent to which micrometeoroid scatter can be modulated and corrected by EFC. But independent reviewer Stuart Shaklan asserted that "while the diffraction component of a micrometeoroid impact is as controllable as any other diffraction component, if it arises from holes more than a micron or two deep, then it will be uncontrollable." [40] These assertions are supported by **Fig 20** which shows that it is easier to correct for smaller contamination particles than for larger particles.

6 Polarization Leakage [7]

Starlight arriving at the telescope entrance aperture has random polarization. In the HWO EAC1 design, this light is separated into orthogonal S and P linearly polarized beams. The two polarization states go to separate coronagraph channels. These two states have zero mutual coherence. That is, even for τ=0, the temporal coherence, γ, is zero, regardless of the bandwidth. Unfortunately, no polarization separation is perfect; there will always be some leakage. Leakage is quantified by the fraction of light going into the unwanted channel and referred to as the extinction ratio. For intensity, the extinction ratio is typically 10^{-4} and the field strength is the square root. This assessment defined the extinction ratio for fields as ϵ≃0.01.

Thus, the S channel coronagraph will have P polarization contamination field with ~ 1% relative strength. **Fig 25** illustrates this in a highly simplified way, ignoring all other optics except the telescope's primary mirror, M1, and the "analyzer" which selects the S polarized beam for this channel.

Figure 25 describes the contributors to the speckle field under the planet signal (PSF core). The nominal field under the PSF core is labeled S_{sp}, ("specular" S-polarized beam) for which this channel was intended. Other contributions include scattered light and polarization leakage. The field strength for S and P polarizations are labeled as simply S or P. The subscripts differentiate between specular (sp) and narrow angle scatter (NAS). The P light in this channel is suppressed by the analyzer down to an extinction ratio of ϵ.

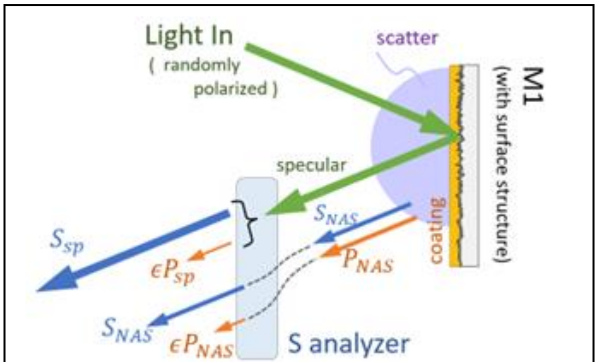

Fig 25: Simplified diagram showing light arriving under the PSF core after reflection from the M1 mirror and passing through an analyzer that nominally selects the S state of polarization.

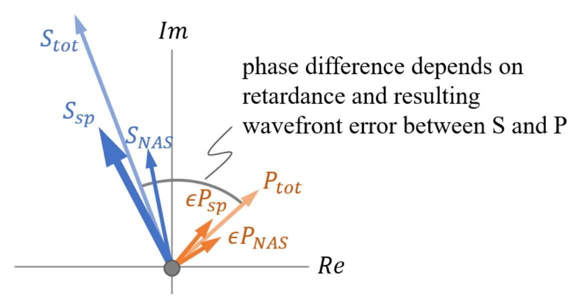

Fig 26: High-retardance case between nominal S field and leakage P field. Subscript "sp" stands for specular and "NAS" stands for Narrow Angle Scatter. Each phasor is the mean field over the core region over an integration time. The leakage P field is reduced by extinction ratio ϵ going through the S analyzer.

In the FRN error budget, polarization leakage contributes to both Average Raw Contrast (through Shot noise) and Speckle Contrast Stability. And it is in both the modulated and unmodulated sub-branches of raw contrast. (**Fig 3**) The reason for the contribution to both sub-branches is because of phase retardance between the S and leakage P components. **Figure 26** shows a hypothetical case where the retardance is high, near 90 degrees, between the S and leakage P fields. In this case the P-field cannot be modulated. But, in EAC1, the angles of incidence are small, and the retardance is very small, on the order of a few milli-degrees. Thus, for EAC-1, the P field can be modulated. The EFC wavefront control process detects the majority field, S, and applies correction to remove it. In so doing it corrects the P leakage "collaterally", since there is little retardance, and the same correction that reduces S will also reduce P (the phasors are near parallel).

The worst-case contribution of Polarization Leakage to Total Raw Contrast was calculated, assuming a 1% E-field leakage (ϵ) and no EFC correction. For the FRED® Case 1 model with 250,000 ppt contrast (τ_{NAS}) at the IWA, the worst case of unmodulated contrast from Polarization Leakage would be 25 ppt.

$$C_{P\ leakage} = |P_{NAS}|^2 = \left|\epsilon\sqrt{\tau_{NAS}}\right|^2 \simeq 25\text{ ppt}$$

P_{NAS} is the NAS E-field contribution from the P polarization state leaking into a coronagraph channel designated for the S polarization state – which is greater than this assessment's 20 ppt error budget allocation. Fortunately, designing an optical system with minimal retardance will reduce this error source contribution.

The contribution of Polarization Leakage to Contrast Stability, because it is self-coherent and contributes to the heterodyne mixing term, also depends on retardance.

$$\Delta C_p \simeq 2\, P_{NAS}\, \Delta P_{NAS} \simeq 2\, \epsilon\sqrt{\tau_{NAS}}\, \Delta P_{NAS} \simeq 10\, \Delta P_{NAS}$$

If there is no retardance, then to keep Contrast Stability below a nominal 5 ppt, the polarization leakage field must be stable to < 0.5 ppt. Again, a system with minimal retardance will relax this specification.

7 Summary and Findings

This paper summarizes a five-year assessment into the impact of near-angle scatter (NAS) on a coronagraph's ability to detect an exo-Earth. The assessment was conducted using a science-driven systems-engineering methodology. A team of subject matter experts from relevant disciplines (systems engineering, coronagraphy, straylight, coating, micrometeoroid, etc.) was assembled to derive physical optical surface specifications from science requirements.

A raw contrast error budget was developed for characterizing Earth-like planets around Sun-like stars with allocations assigned to sources of NAS, including correlated surface structure, uncorrelated microroughness and coating structure, contamination, micrometeoroid impacts and polarization. (Diffraction from segment edges and ghost reflections were beyond the scope of this assessment.) Specifications for correlated surface structure and roughness were derived from the error budget contrast allocations using Rayleigh-Rice Vector Scatter Theory and Generalized Harvey-Shack Scalar Scatter Theory. Error budget allocations were categorized into modulated (can be corrected via Electric Field Conjugation) and unmodulated (cannot be corrected).

An analytical relationship was derived between coronagraph contrast and Bidirectional Reflectance Distribution Function (BRDF), which flowed naturally to a relationship between coronagraph contrast and wavefront Power Spectral Density (PSD). Using these relationships and Photon Engineering's FRED® software, a parametric scattered light analysis was conducted of the Habitable Worlds Observatory (HWO) Exploratory Analytical Case #1 (EAC-1) coronagraph as a function of optical surface PSD (correlated and uncorrelated structure), microroughness, contamination and polarization.

In the final report to the NESC, the Assessment Team identified multiple findings:

1. Post-EFC (i.e. corrected) modulated residual scattered starlight from correlated surface structure and unmodulated residual scattered starlight contribute contrast into the 'Total Raw Contrast' portion of the random noise branch of the contrast error budget.
2. Modulated and unmodulated scattered starlight contribute noise into the Contrast Stability branch of the coronagraph flux ratio noise (FRN) error budget.

$$|E+\Delta E|^2 = |E|^2 + |\Delta E|^2 + 2\,\mathscr{R}\{E^{*}\cdot\Delta E\}$$

Coherent spatially correlated scattered light contributes to the ΔE term. And coherent diffuse scattered light adds to the E term and acts as an amplifier in the cross-term.

3. Scattered light metric BRDF/BSDF can predict contrast leakage from scatter transmittance:

$$\tau_{\mathrm{NAS}}\,[\mathrm{ppt}] = \mathrm{BRDF}\ \cdot\ \Omega_{core}$$

4. Using Rayleigh-Rice Vector Scatter Theory, specifications were defined for long-spatial frequency correlated structure (angular scatter into dark hole) and mid-spatial frequency correlated structure (angular scatter beyond dark hole outer working angle) for a 'composite' surface based on the contrast error budget for three temporal states:
    - Initial Post-EFC is caused by Static Correlated Structure
    - Drift Field Mean is caused by Slow Correlated Structure
    - Jitter Field Variance is caused by Fast Correlated Structure
5. Slow drift (i.e. thermal) is 10X more important than fast periodic motion (i.e. mechanical).
6. Coating microstructure should not be a significant source of diffuse straylight contrast because its correlation length is too small.
7. Native surface microstructure can be a significant source of diffuse straylight contrast depending on its correlation length.

8. The study does not make an assessment as to the extent to which diffuse scatter from microstructure can be modulated and corrected by EFC. And while interesting, it may also be pure coincidence that FRED® predicts dark hole contrast uncorrelated microstructure consistent with the reported unmodulated noise floor of several coronagraph test beds.
9. Straylight analysis codes can be a valuable modeling tool; they can predict both energy in the dark hole before correction from correlated surface structure (as described by a PSD) and from potentially uncorrectable uncorrelated surface structure (also described by a PSD).
10. Not every surface requires the same specification. Modeling indicates that each surface contributes scatter differently depending upon its solid angle to the dark hole. The smallest surfaces and surfaces closest to the focal plane mask contribute the most scatter.
11. Surface contamination may be a significant contributor to Raw Contrast Shot Noise. Fortunately, because different surfaces contribute differently to total contrast, not every surface will require CL-75.
12. The study does not make an assessment as to the extent to which contamination scatter can be modulated and corrected by EFC. Balasubramanian et al. (2009) concluded that scatter due to contamination was mostly uncontrollable.
13. Micrometeoroid impacts may be a significant source of near-angle scatter – particularly if they are large or numerous. But the study does not make a definitive micrometeoroid impact specification – in part because impact morphology is complex and there is no agreed method for assessing their contribution to dark hole contrast.
14. The study does not make an assessment as to the extent to which scatter from micrometeoroid impacts can be modulated and corrected by EFC.

15. Finally, as long as the telescope/coronagraph optical system retardance is low, Polarization Leakage should not be a significant contributor to either Raw Contrast or Contrast Stability.

REFERENCES

1. National Academies of Sciences, Engineering, and Medicine, “Pathways to Discovery in Astronomy and Astrophysics for the 2020s,” Washington, DC: The National Academies Press, (2021) https://doi.org/10.17226/26141.
2. Richard N. Pfisterer, James E. Harvey, James B. Breckinridge, "The role of narrow-angle forward surface scatter and particulate scatter in exoplanet exploration," Proc. SPIE 10698, Space Telescopes and Instrumentation 2018: Optical, Infrared, and Millimeter Wave, 106985F (6 July 2018); https://doi.org/10.1117/12.2314229
3. Ruane, Garreth, et. al., “Microelectromechanical deformable mirror development for high-contrast imaging, part 2: the impact of quantization errors on coronagraph image contrast”, arXiv.2010.03704v1, 8 Oct 2020.
4. Byoung-Joon Seo, et. al., "Testbed demonstration of high-contrast coronagraph imaging in search for Earth-like exoplanets," Proc. SPIE 11117, Techniques and Instrumentation for Detection of Exoplanets IX, 111171V (16 September 2019); doi: 10.1117/12.2530033
5. Byoung-Joon Seo, et. al., "Hybrid Lyot coronagraph for WFIRST: high-contrast broadband testbed demonstration," Proc. SPIE 10400, Techniques and Instrumentation for Detection of Exoplanets VIII, 104000F (1 September 2017); doi: 10.1117/12.2274687
6. Nemati, Stahl, "Leveraging the Roman coronagraph approach for the HWO error budget," Proc. SPIE 13092, (23 August 2024); https://doi.org/10.1117/12.3021198
7. Nemati, Stahl, "Flowdown of the HWO error budget to mirror specifications constraining diffuse narrow angle scatter," Proc. SPIE 13623, (18 September 2025); https://doi.org/10.1117/12.3064451
8. Stover, John C, Optical Scattering Measurement and Analysis, Section 6.2, McGraw-Hill, New York, NY, 1990
9. Stahl, "Assessment of near-angle scatter on exo-Earth coronagraphy," Proc. SPIE 12676, (4 October 2023); https://doi.org/10.1117/12.2676543
10. Stahl, Smith, Nemati, "Impact of near-angle scatter on exo-Earth coronagraphy," Proc. SPIE 13092, (23 August 2024); https://doi.org/10.1117/12.3021201
11. Stahl, Smith, Nemati, "Mirror surface contamination specification derived from coronagraphy scatter error budget allocation," Proc. SPIE 13129, (1 October 2024); https://doi.org/10.1117/12.3028546
12. Nemati, Bijan, H. Philip Stahl, Mark T. Stahl, Garreth J. Ruane, Leah J. Sheldon, "Method for deriving optical telescope performance specifications for Earth-detecting coronagraphs," J. Astron. Telesc. Instrum. Syst. 6(3), 039002 (2020), doi: 10.1117/1.JATIS.6.3.039002.
13. Nemati, Stahl, Stahl, Shaklan, "Effects of space telescope primary mirror segment errors on coronagraph instrument performance", Proc. SPIE 10398, (5 September 2017); doi: 10.1117/12.2273072; http://dx.doi.org/10.1117/12.2273072
14. L. Leboulleux et al., “Pair-based Analytical model for Segmented Telescopes Imaging from Space for sensitivity analysis,” Journal of Astronomical Telescopes, Instruments, and Systems 4(3), 1 (2018).

15. G. Ruane et al., “Vortex coronagraphs for the Habitable Exoplanet Imaging Mission concept: theoretical performance and telescope requirements,” Journal of Astronomical Telescopes, Instruments, and Systems 4(1), 1 (2018) [doi: https://doi.org/10.1117/1.JATIS.4.1.015004].

16. L. E. Coyle et al., “Large ultra-stable telescope system study,” in UV/Optical/IR Space Telescopes and Instruments: Innovative Technologies and Concepts IX, SPIE 111150R, 27 (2019) [doi: https://doi.org/10.1117/12.2525396].

17. John Krist, Private Communication 11/14/24

18. Kern, “Coronagraph Sensitivities (LEM)”, Internal Briefing, 5 Mar 25

19. B. Nemati, J. J. E. Krist, I. Poberezhskiy, B. D. B. Kern, I. Poberezhskiy, and J. J. E. Krist, “Analytical performance model and error budget for the Roman coronagraph instrument,” J Astron Telesc Instrum Syst, vol. 9, no. 3, pp. 1–36, 2023, doi: 10.1117/1.JATIS.9.3.034007.

20. C. C. Stark et al., “ExoEarth yield landscape for future direct imaging space telescopes,” vol. 5, no. 2, 2022, doi: 10.1117/1.JATIS.5.2.024009.

21. A. Give’on, B. D. Kern, and S. Shaklan, “Pair-wise, deformable mirror, image plane-based diversity electric field estimation for high contrast coronagraphy,” in Techniques and Instrumentation for Detection of Exoplanets V, SPIE, Sep. 2011, p. 815110. doi: 10.1117/12.895117.

22. Give’on, Kasdin, Vanderbei and Avitzour, “High-Frequency folding and optimal phase conjugation for high-contrast adaptic optics”, SPIE Proc 5490, Advancements in Adaptive Optics, (2004) doi: 10.1117/12.551576

23. Give’on, Kasdin, Vanderbei & Avitzour, “On representing and correcting wavefront errors in high-contrast imaging systems” JOSA Vol.23, No.5, p.1063, 2006.

24. Allen, Chris, “Surface Scattering”, Course website URL people.eecs.ku.edu/~callen/823/EECS823.htm

25. Chris A. Mack, "Reducing roughness in extreme ultraviolet lithography," J. Micro/Nanolith. MEMS MOEMS 17(4) 041006 (7 August 2018) https://doi.org/10.1117/1.JMM.17.4.041006

26. L. V. Rodriguez de Marcos, V. D. Wheeler, M. F. Batkis, J. G. del Hoyo, E. N. Jin, S. G. Walton, E. J. Wollack, M. A. Quijada, and D. R. Boris, "Passivation of aluminum mirrors with SF6- or NF3-based plasmas", Optical Materials Express Vol. 13, Issue 11, pp. 3121-3136 (2023); https://doi.org/10.1364/OME.499273

27. Manuel A. Quijada, Javier G. Del Hoyo, Luis V. Rodriguez De Marcos, Edward J. Wollack, Mateo F. Batkis, Devin M. Lewis, Tanner D. Rydalch, David D. Allred, "Far-ultraviolet optical properties and performance of physical vapor deposited aluminum mirrors protected with XeLiF and XeMgF2," J. Astron. Telesc. Instrum. Syst. 11(4) 042209 (30 June 2025) https://doi.org/10.1117/1.JATIS.11.4.042209

28. Luis Rodriguez de Marcos, Mateo Batkis, Javier Del Hoyo, Edward Wollack, H. Philip Stahl, and Manuel Quijada, “Surface Characterization of Al protected with XeLiF and XeMgF2 (I): PSD and ACF characterization”, in-process.

29. Luis Rodriguez de Marcos, Mateo Batkis, Javier Del Hoyo, Edward Wollack, H. Philip Stahl, and Manuel Quijada, “Surface Characterization of Al protected with XeLiF and XeMgF2 (II): Scattering and surface plasmon characterization”, in-process.

30. Fest, Eric C., Stray Light Analysis and Control, SPIE Press, 2013

31. Pfisterer, Richard N., James E. Harvey, James B. Breckinridge, "The role of narrow-angle forward surface scatter and particulate scatter in exoplanet exploration," Proc. SPIE 10698, Space Telescopes and Instrumentation 2018: Optical, Infrared, and Millimeter Wave, 106985F (6 July 2018); https://doi.org/10.1117/12.2314229

32. Kunjithapatham Balasubramanian, Stuart Shaklan, Amir Give'on, "Stellar coronagraph performance impact due to particulate contamination and scatter," Proc. SPIE 7440, Techniques and Instrumentation for Detection of Exoplanets IV, 74400T (25 August 2009); https://doi.org/10.1117/12.825182

33. John Krist, Private Communication 14 Nov 2024

34. Kern, “Coronagraph Sensitivities (LEM)”, Internal HWO Briefing, 5 Mar 25

35. Krist, “Integrating STOP and Diffraction Modeling”, Internal HWO Briefing, 5 Mar 25

36. Kunjithapatham Balasubramanian, Stuart Shaklan, Amir Give'on, "Stellar coronagraph performance impact due to particulate contamination and scatter," Proc. SPIE 7440, Techniques and Instrumentation for Detection of Exoplanets IV, 74400T (25 August 2009); https://doi.org/10.1117/12.825182

37. John Krist, Private Communication, 18 Nov 2025

38. Iyer, et. al., “Glass Surface Spall Size Resulting from Interplanetary Dust Impacts”, IEEE, 978-1-4799-5380-6, 2015.

39. J. D. Gaskill, “Linear Systems, Fourier Transforms, and Optics,” John Wiley &Sons, Inc., New York, 1978.

40. Stuart Shaklan, Private Communication, 30 Sept 2025

APPENDIX A: Science Requirements to Coronagraph Flux Ratio Error Budget

Appendix A summarizes the methodology used to flow down the Habitable World Observatory science requirements to a flux contrast ratio error budget – as published in SPIE proceedings paper Reference 6 "Leveraging the Roman coronagraph approach for the HWO error budget" by Nemati and Stahl, 2024.

A.1 Flux Ratio

Detecting and characterizing an exoplanet requires measuring its signal in the dark hole against a background. The signal is proportional to the planet flux ratio, which is defined as the ratio of the flux from the planet, as received at the telescope, relative to the star. Traub and Oppenheimer **[A-1]** give a simple expression to estimate the flux ratio:

$$\xi = A_g \, \phi(\alpha) \, r_p^2 \, a^{-2}$$

where A_g is the geometric albedo and $\phi(\alpha)$ is the geometric phase function, giving the variation of the light scattered towards the observer as a function of the orbital phase angle α. **(Fig. A-1)** The last two factors are the planet radius r_p and semi-major axis a. For the Earth, $r_p^2 a^{-2}$ is 1814 ppt (parts per trillion). If the exoplanet is taken as a Lambertian sphere, the phase function is given by Traub and Oppenheimer **[A-1]**:

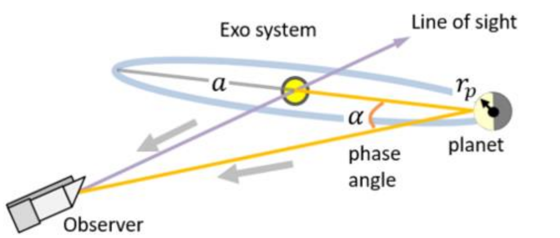

Fig. A-1: Geometrical elements affecting reflected light flux ratio include the planet radius, the phase angle, the distance to the observer, and the semimajor axis.

$$\phi(\alpha) = \frac{sin(\alpha) + (\pi - \alpha)\, cos(\alpha)}{\pi}$$

At maximum elongation, i.e. when $\alpha = \pi/2$, $\phi \simeq 1/\pi$. At smaller separations, the phase function rises, but the advantage is offset by the increase in speckle from the star. A practical optimum can be selected, and for this paper we choose 80 degrees, at which $\phi(\alpha) \simeq 0.4$.

It is noteworthy here that the appropriate albedo to use, for reflected light detection, is the *geometric* albedo, and not the Bond albedo. The latter is the ratio of the light incident on the planet that does not heat up the planet. This measure is appropriate for detection of the planet as a blackbody in the infrared, but not for reflected light observations. De Cock, et al. **[A-2]** use EPOXI mission data and obtain a range of geometric albedo values, from 0.176 to 0.255, for the Earth. The higher value is from polar measurements while the lower is from equatorial measurements. This data supports the adoption of $A_g = 0.2$ as the representative geometric albedo value for an exo-Earth for error budgeting purposes. The combination of such a low albedo, small size of the Earth, and its proximity to the Sun makes the goal of direct imaging an exo-Earth analog challenging.

In planning observations, one must also take into account the relatively strong dependence of the reflected light signal on the planet's orbital phase angle at the observation epoch. As the phase angle becomes smaller, the planet becomes brighter. But the apparent angular separation between the planet and the star gets smaller and there is a limit as to how small this angle can be for detection. Coronagraphs have a minimum inner working angle (IWA) – inside of which the star's light cannot be blocked and the planet not detected. Also, when looking at star systems that are further away to increase the sample size, the minimum working phase angle increases. **Fig. A-2** illustrates this for two different IWA cases. The shaded region under each curve is the phase angle range that is *excluded*.

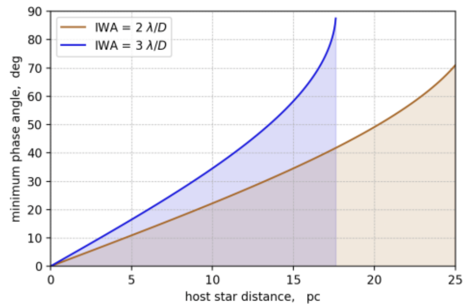

Fig. A-2: For a coronagraph with a given inner working angle (IWA), observing a planet at smaller working angles becomes harder for farther targets. Two cases are shown in this figure, one with a coronagraph with inner working angle (IWA) of 2 λ/D and the other with IWA of 3 λ/D. In each case, the inaccessible phase angles are shaded.

Figure A-3 shows the dependence of flux ratio on orbit phase angle. At quadrature phase ("half-moon", at 90 degrees) the flux ratio is only 115 ppt. At 80 degrees it rises to about 150 ppt. Going to smaller phase angles can more than double the flux ratio, but, as shown in **Fig. A-2**, these phase angles are not allowed for stars that are farther away.

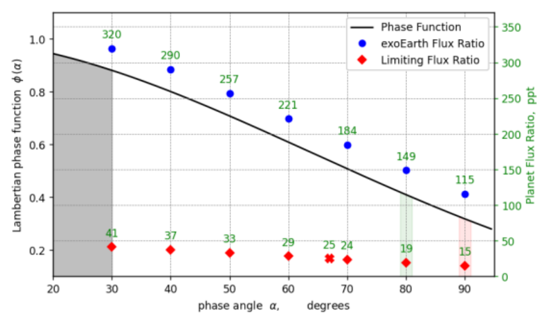

Fig A-3: The expected flux ratio for an exo-Earth is calculated assuming a geometric albedo, the phase angle, the phase function. For $A_g = 0.2$, the phase function for a Lambertian sphere is plotted as a black line (left axis), while flux ratios (in ppt) are plotted as points against the right axis. The blue circles correspond to an exo-Earth. The green shaded phase angle value of 80 degrees is adopted because it is the smallest phase angle that can be observed with a 3λ/D inner working angle coronagraph for a star system at 15 to 17 parsecs. Therefore, it is the limiting case for an Earth-like planet around a Sun-like star. The red diamonds indicate the flux ratio needed to detect a planet that is 60% the size of Earth and a distance of 1.67 AU from its star. **[A-3]**

In **Fig A-3**, we make a distinction between true exo-*Earths*, which pertain to observing *our* solar system from a few parsecs away, and planets that are *roughly* Earth-like, with sizes and orbital radii covering a wider range. Stark et al. **[A-3]**, for example, considers an appropriate target for completeness to be a planet with flux ratio of 25 ppt (Δmag = 26.5). This case can be interpreted either as a low-flux ratio (e.g. crescent) phase of a larger planet or that of a smaller one with a longer period. If interpreted as the latter, it could be a planet at the edge of their allowed exoplanet phase space: radius equal to 0.6 time that of the Earth, and orbital radius of 1.67 AU. For this combination, the geometric factor $r_p^2\ a^{-2}$ is 7.75 times smaller than for the Earth. Since they also assume a geometric albedo of 0.2 and Lambertian scatter, their flux ratio corresponds to a phase angle of about 67 degrees. **Figure A-3**Error! Reference source not found. shows, in red diamonds, t he flux ratios vs. phase angle for this limiting case and highlights with an "X" the reference point at 25 ppt / 67 degrees.

The assessment assumes a true exo-Earth target, adopting 150 ppt as the target flux ratio for error budgeting purposes. However, it is an important caveat that the number of targets at this flux ratio may be very small.

A.2 Signal to Noise Ratio

When the planet's location is not known a priori to adequate accuracy, the photometric signal to noise ratio must be high enough to avoid false positives. Suppose that the dark hole has an IWA of 3 λ/D and an outer working angle (OWA) of 10 λ/D; and, that the core of the PSF covers an area of $(\lambda/D)^2$. The speckles in the dark hole, which arise from diffractive effects, will all be approximately the same size as the PSF core, so the dark hole contains approximately 286 speckles, each $(\lambda/D)^2$ in size. In this context the speckles are '*residual'*, i.e. after some type of PSF subtraction or differential imaging. Therefore, for the purposes of statistical analysis, the speckle intensities, sampled within random $(\lambda/D)^2$ areas, are assumed to be normally distributed. This allows one to write a simple expression for the "false alarm" probability (P_{FA} or FAP) that, across N_{obs} observations (imaging instances during a mission) culminating in a single final dark hole image with N_{DH} speckles, there would be one dark hole speckle whose intensity would exceed the standard deviation of the speckles by a factor greater than a given SNR. Such an expression ties the choice of SNR systematically to false positive rejection. This probability is given by:

$$P_{FA} = 1 - \left(1 - \frac{1}{2}\, erfc\left(\frac{SNR}{\sqrt{2}}\right)\right)^{N_{obs} \cdot N_{DH}}$$

where *erfc* is the complementary error function.

Assuming a mission goal of searching 100 planetary systems for exo-Earths with a FAP of < 1%, requires a probability of less than 1% that a single 'residual' speckle in any of the 100 dark hole images reaches a SNR greater than our required SNR. **Fig A-4** shows the evaluation of the above expression for various cases: per single λ/D sized speckle ($N_{obs} = 1, N_{DH} = 1$), per single dark hole ($N_{obs} = 1, N_{DH} = 286$), and per single mission ($N_{obs} = 100, N_{DH} = 286$). The third case is the most important and shows that a SNR greater than 5 is required so as not to exceed the allowable FAP.

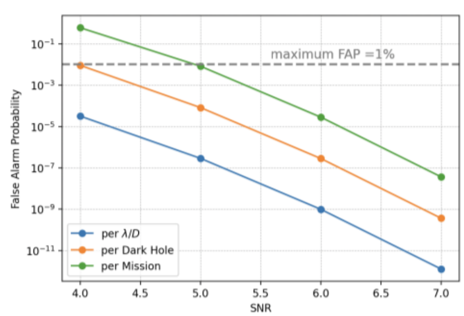

Fig A-4: False alarm probability (FAP) vs. the SNR setting, for three cases: (a) a single sample of one λ/D speckle, (b) one dark hole, and (c) 100 dark holes over the course of a mission. The dashed line represents a maximum false alarm probability of 1%. For a mission, the requirement that the FAP be less than 1% means the detection SNR requirement must be at least 5.

It is helpful to visualize the SNR and false positive probabilities. **Fig A-5** shows a number of SNR cases, where a sample of pixels the size of the dark hole (in λ/D sized speckles) contains one signal pixel with the stated SNR, from 3 to 7.

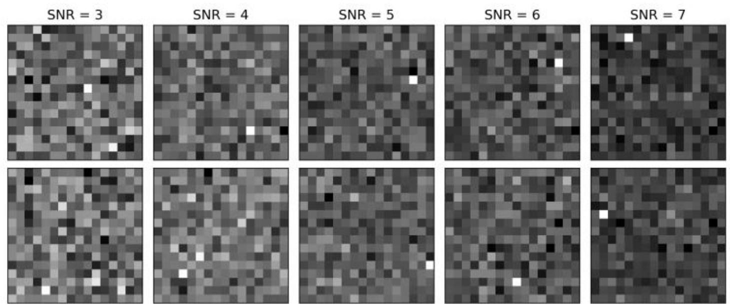

Fig A-5: Each square represents the number of core-sized speckles in HWO's dark hole. Each square represents a single dark hole image with one signal pixel at a given SNR. SNR cases 3 through 7 are displayed in columns, with two instances each. False alarm probability increases as the number of dark holes increases (see **Fig A-4**).

Fig A-4 shows that to maintain FAP below 1% over the mission, the minimum SNR needed is 5. But this is for the 'mean' expected signal and the 'mean' expected noise. In an ensemble of observations, 50% of the cases would result in SNR lower than this average value. Therefore, a SNR must be selected that provides margin. A reasonable approach is to set a requirement on the maximum fraction of cases that are allowed to fail reaching the desired SNR. We will call this f_s. If the noise that accompanies the signal is Gaussian, then the SNR distribution has a standard deviation of unity and an expression can be written for a target SNR value (SNR_{tar}), above the desired SNR value (SNR_{min}), which ensures that the goal SNR fails to be reached for no more than f_s fraction of attempts.

$$f_s = \frac{1}{2} erfc\left(\frac{SNR_{tar} - SNR_{min}}{\sqrt{2}}\right)$$

Fig A-6, shows that a SNR of 7 is required to keep $f_s < 2\%$ for a SNR of 5. The left side shows that a SNR margin of +2 is required to keep $f_s < 2\%$. The right side shows a Gaussian SNR distribution, centered at SNR=7, and the 2-percentile lower region, ending in SNR=5, is shaded. Note, from a photometry standpoint, a SNR of 7 means a fractional error of 1/7, or 14%, can be expected on average. Also note that this SNR is independent of flux ratio.

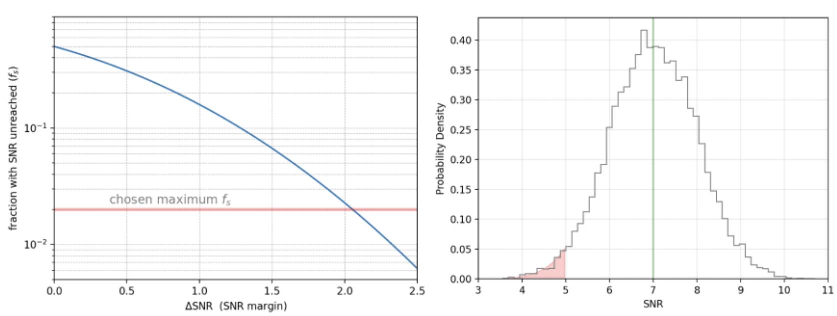

Fig A-6: Choosing a ΔSNR margin can ensure that no more than a fraction, f_s of the observations end up with SNR below the desired value. Here, f_s has been set to 2%, which, per the left graph, requires ΔSNR>2. The Gaussian probability density histogram on the right has been shaded in its lowest 2%, confirming that a target SNR of 7 is needed to ensure a mission level FAP of < 1%.

A.3 Flux Ratio Noise Error Budget

Since the flux ratio is the basic measurement in direct imaging, the error budget should be based on the flux ratio noise (FRN). [A-4] As discussed above, the total allowable FRN for HWO is set to be 150 ppt by the bounding observing constraint of 80 degrees phase angle (Error! Reference source not found.) and SNR of 7, for a total flux ratio noise allocation of 21.4 ppt. This allocation is then split into a budget with three major branches: random noise, speckle noise, and calibration errors. [A-4] Random noise includes shot noise and detector errors. Speckle noise is the residual error after imperfect differential imaging or PSF subtraction. Finally, calibration error pertains to relating the estimated signal, in its native units of counts (photoelectrons) to planet flux ratio. This does not affect the significance of the signal but is a systematic error in the conversion to flux ratio.

An important practical consideration is the time it takes to reach the target SNR. This time depends on the signal rate from the planet, r_{pl}, in electrons per second and the noise variance rate r_n (variance divided by the integration time). It also depends on the spatial variance $\sigma_{\Delta I}^2$ of the differential image, that is, the residual speckle variance. This variance in general does not, like shot noise, grow proportionally with integration time: in this case it is the standard deviation that grows linearly with time. Thus, it is helpful to define a "residual speck rate" $r_{\Delta I} \equiv \sigma_{\Delta I}/t$, where t is the integration time. [A-4, A-5] In terms of these variables, the time needed to reach a target SNR is given by:

$$t_{SNR} = \frac{\mathrm{SNR}^2\, r_n}{r_{pl}^2 - \mathrm{SNR}^2\, r_{\Delta I}^2}$$

The residual speckle noise $\sigma_{\Delta I}$ is a decisive attribute of direct imaging performance and will eventually dictate what architectures are feasible for HWO and which ones are not. But with some basic assumptions we can come up with a top-level allocation for it.

The assumptions that go into the random noise calculation are summarized in Table A-1. We also assume a low noise detector such as an EMCCD in photon counting mode.

Table A-1: Assumption for forward calculation of random noise.

Host Star V mag	5.9	mag	Band Center	550	nm
Host star distance	16.0	pc	Band Width	20%	
Planet Flux Ratio	148.7	ppt	Configuration	IMG VVC6	
Planet phase angle	80.0	deg	Core Throughput	25.7%	
Planet radius	1.0	$R_\oplus$	Total Throughput	9.4%	
Planet SMA	1.0	AU	Planet Working Angle	3.26	λ/D
Exo Zodi level	1.0	x solar	Raw Contrast	301	ppt

Following the approach in Reference [A-5], and using the assumptions above, **Fig. A-7** plots the total flux ratio noise of different source that can be assigned to the 21.4 ppt allocation as a function of integration time. Note that total random noise goes down as $t^{1/2}$.

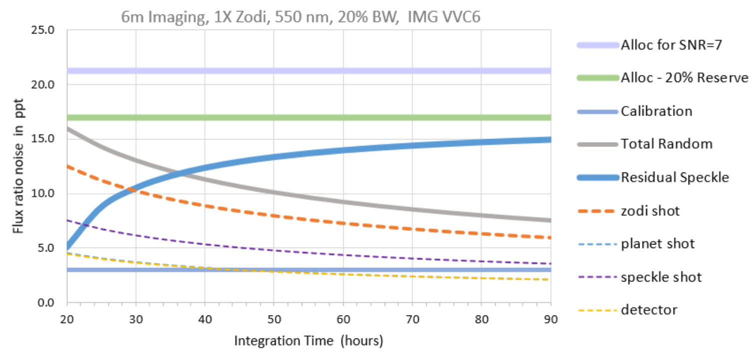

Fig. A-7: Integration time can be defined by balancing Total Random Noise with Residual Speckle. Calculation assumes a relatively optimistic set of characteristics as obtained from a vector-vortex charge 6 coronagraph.

Setting aside a reserve of 20% and 2% for calibration errors, the remainder, in a root-sum-square (RSS) sense, is what can be allocated to residual speckle. It can be seen in **Fig. A-7** that the cross-over point where the allocations to random noise and residual speckle are equal is at about 34 hours of integration. At 40 hours, random noise reduces to 11.3 ppt, allowing for 12.4 ppt of residual speckle. Going longer will afford more residual speckle, but with diminishing returns. It is noteworthy that the largest contribution to the random noise is exo-Zodi, and for this a rather optimistic value of 1x solar is assumed. If the universe fails to cooperate, there will be a large impact on allowable errors and the error budget. Please note that **Fig. A-7** calculations are for direct imaging. The time to SNR for spectroscopy will be much longer.

Fig. A-8 shows the top-level error budget for HWO direct imaging of an exo-Earth with 150 ppt of flux ratio in the visible (550 nm, 20% band). Additionally, it is assumed that, beyond any benefit from stability within a differential imaging scenario, there is an additional factor (f_{pp}) of 5x improvement from post-processing algorithms. Reference A-4 describes the factor κ_c which is a conversion factor from residual speckle standard deviation (ΔC) and its contribution to flux ratio noise ($\delta\xi$).

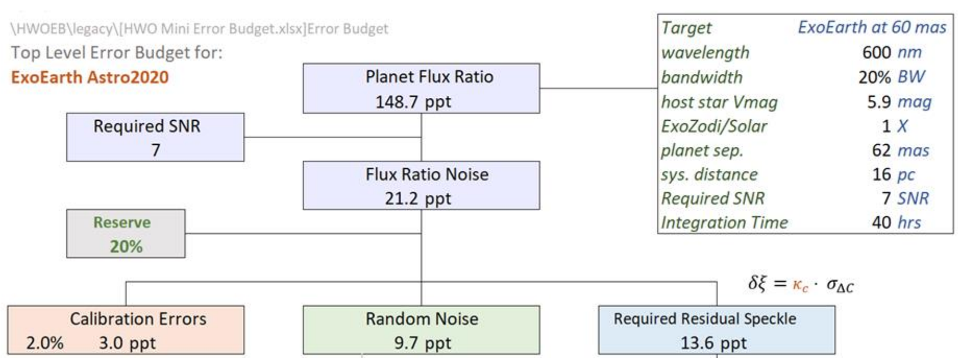

Fig. A-8: Top level error budget for direct imaging of an exo-Earth. The calibration branch allocation is 2% of the target flux ratio. The Random Noise allocation is from the "All Random" curve in **Fig. A-7**, for 40 hrs of integration. The reserve of 20% is a conventional engineering choice. The residual speckle allocation is obtained from subtracting the Calibration and Random Noise allocations from the Flux Ratio Noise total, in quadrature.

For completeness, **Fig. A-8** shows the top-level error budget for HWO direct imaging of a limiting-case exo-planet with 33 ppt of flux ratio in the visible (550 nm, 20% band). To achieve a SNR of 7 requires an integration time of 300 hrs.

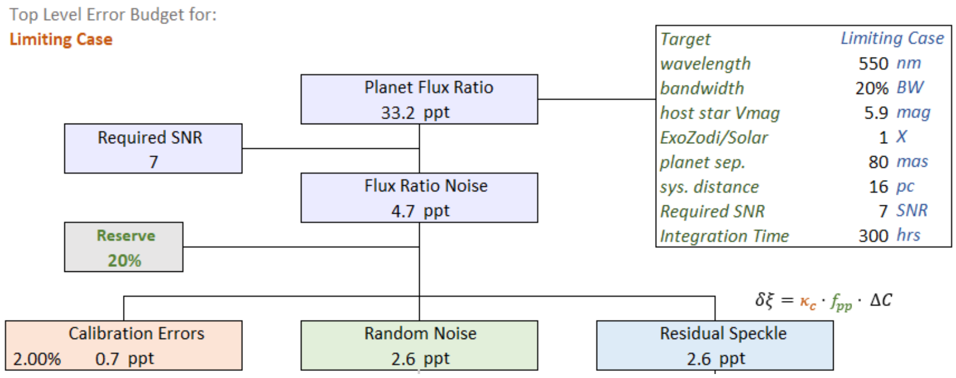

Fig. A-9: Top level Flux Ratio Noise error budget allocations for limiting case exo-planet.

<u>APPENDIX A: References</u>

A-1 Traub, Oppenheimer, "Direct imaging of exoplanets", Exoplanets, Seager, ED, Tucson AZ, Univ of Arizona Press, 2010, pp 111-156.

A-2 R. De Cock, T. A. Livengood, D. M. Stam, C. M. Lisse, T. Hewagama, and L. D. Deming, "Terrestrial Planet Optical Phase Curves. I. Direct Measurements of the Earth," Astron J, vol. 163, no. 1, p. 5, 2022, doi: 10.3847/1538-3881/ac3234.

A-3 C. C. Stark et al., "ExoEarth yield landscape for future direct imaging space telescopes," vol. 5, no. 2, 2022, doi: 10.1117/1.JATIS.5.2.024009.

A-4 B. Nemati, J. J. E. Krist, I. Poberezhskiy, B. D. B. Kern, I. Poberezhskiy, and J. J. E. Krist, "Analytical performance model and error budget for the Roman coronagraph instrument," J Astron Telesc Instrum Syst, vol. 9, no. 3, pp. 1–36, 2023, doi: 10.1117/1.JATIS.9.3.034007.

A-5 B. Nemati, H. P. Stahl, M. T. Stahl, G. J. Ruane, and L. J. Sheldon, "Method for deriving optical telescope performance specifications for Earth-detecting coronagraphs," *J Astron Telesc Instrum Syst*, vol. 6, no. 03, Aug. 2020, doi: 10.1117/1.jatis.6.3.039002.

APPENDIX B: Scattered Light Models and Mathematics

Given that coronagraph scientists typically use diffraction propagation models to predict contrast leakage, Appendix B provides a tutorial overview of scattered light then summarizes models and mathematics used to describe the physical production of scattered light and its connection to coronagraph contrast leakage via the mathematics of Contrast Throughput (τ), BRDF/BSDF (bidirectional reflectance/scatter distribution function) and PSD (power spectral density). Appendix B merges content from three SPIE proceedings papers: REF 9. "Assessment of near-angle scatter on exo-Earth coronagraphy," 2023; REF 10. "Impact of near-angle scatter on exo-Earth coronagraphy," 2024; and REF 7. "Flowdown of the HWO error budget to mirror specifications constraining diffuse narrow angle scatter," 2025.

B.1 Scattered Light

For an ideal telescope/coronagraph system (one with a perfect wavefront, i.e. no aberrations, and no scatter), the telescope produces an ideal point spread function (PSF) of the host star and the coronagraph blocks its light completely, allowing light from the exo-Earth to be detected and characterized. But, even in a perfect system, diffraction produces some leakage. And, in an imperfect system, wavefront or amplitude errors (whose distribution in spatial frequency can be described by their power spectral density – PSD) can scatter light out of the host star's PSF and onto the exo-Earth's PSF (**Fig B-1**). PSD is typically divided into 3 spatial frequency regimes: Low, Mid and High. The low-spatial frequency regime (dominated by figure errors) determines the shape of the PSF core. Mid-spatial frequency errors produce small-angle scatter which broaden the PSF. High-spatial frequency micro-roughness produces wide angle and uniform Lambertian scatter across the entire PSF. **[B-1]**

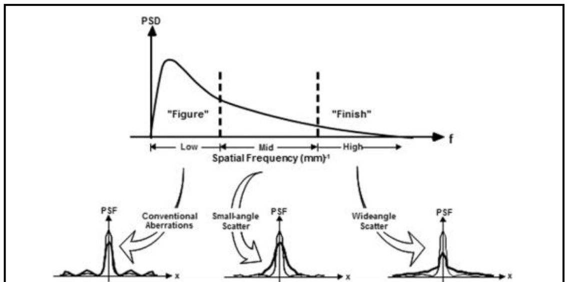

Fig B-1: Surface (or wavefront) spatial frequency error scatters light out of core PSF. **[B-1]**

Surface structure (low, mid, and high) that can be decomposed into specific spatial frequencies scatters (actually diffracts) light out of the PSF to specific angles. These spatial frequencies are referred to as 'correlated' surface structure. Surface structure that cannot be decomposed into specific spatial frequencies diffusely scatters light into all angles. This structure is referred to as 'uncorrelated'. An example of uncorrelated scattering is a Lambertian surface which scatters incident light uniformly into all projected solid angles.

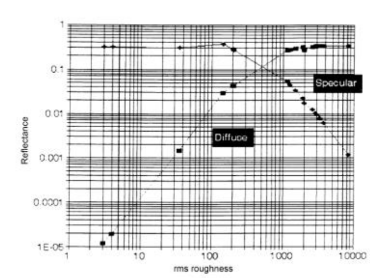

Fig B-2: Conservation of Energy balances Specular and Diffuse Scatter. **[B-2]**

By conservation of energy, assuming no transmission or absorption, all light incident upon a surface comes off of that surface via one of three mechanisms: specular reflection, correlated scatter/diffraction or uncorrelated/diffuse scatter. The amplitude of each component of this reflection depends upon the surface's roughness. (**Fig B-2**) The smoother the surface, the smaller the amplitude of its diffuse scatter. But all surfaces, even super polished surfaces, have some amount of uncorrelated microstructure and thus have some amount of diffuse scatter. **[B-2]**

Because the host star is in the field of view, every optical surface is a scattering source with a direct path to the detector. Host star light directly illuminates the primary mirror. The primary mirror scatters some of that irradiance into an angle which, after reflecting off the secondary mirror spreads energy across the coronagraph dark hole, including in the region of the exo-Earth signal. Next, some the host star light (specular reflection of PM) incident on the secondary mirror is scattered across the PSF and into the dark hole. And so on for the tertiary and quaternary mirrors. At this point it is very important to note that scattered light sums. (**Fig B-3**) It does not root-sum-square (RSS) like wavefront errors. **[B-3]**

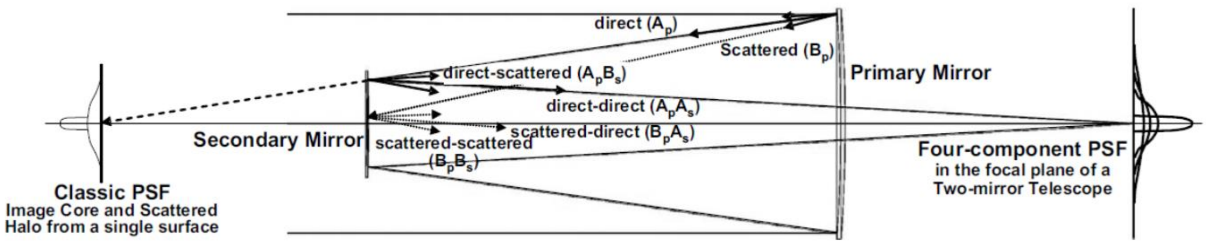

Fig. B-3 Each surface in telescope/coronagraph optical train is an 'in-field' source of near-angle scatter which sums in focal plane. **[B-3]**

It is also important to note that the scattered E-fields are constructively coherent with the leakage E-field. Because the scattered light is from the host star light, there is no phase difference. Because the optical surfaces are very smooth (nanometers rms), the optical path difference is much smaller than the host star light's coherence length (micrometers) – because the coronagraph spectral band is narrow (i.e. < 20%).

Finally, scattered E-fields from the primary mirror are collimated in the dark hole. Consider a single point scatterer on the primary mirror. The secondary and aft optics reimage that scattering source into a conjugate plane in the coronagraph. In **Fig 2**, the pupil mask is located at this plane. And, per **Fig 2**, a diverging point source in the pupil mask plane is collimated, focused, and recollimated into the dark hole. Now consider that the primary mirror's uncorrelated microstructure can be decomposed into billions or trillions of point scatterers each contributing a very small constructively coherent collimated E-field into the dark hole. Similarly, the secondary mirror contributes E-fields, which, while not collimated, have radii on the order of 30 meters.

B.2 Scatter Models

There are two scatter models in common use: Rayleigh-Rice Vector Scatter (essentially the grating equation) and Generalized Harvey-Shack Scalar Scatter (a parametric model). Both models have been used in the past to reliably predict wide angle scatter from as close as a few degrees from a bright source.

B.2.1 Rayleigh-Rice (R-R) Vector Scatter Theory

Rayleigh-Rice is a 'smooth' surface theory. Where 'smooth' is defined to be a surface whose RMS roughness is either smaller than < λ/100 (< ~5 nm rms) **[B-2]** or < λ/1000 (< ~ 0.5 nm rms). **[B-4, B-5]** To first order, R-R vector theory uses the diffraction grating equation to calculate the amount of power at a given wavelength λ that is removed from the PSF into a given scatter angle θ_i by the surface PSD spatial frequency f_x

$$\sin\theta_i = \theta_i = f_x\,\lambda = \frac{\lambda}{d}$$

Scattered light as a function of angle is proportional to the surface's PSD and scales with wavelength. Because diffraction is a physical optic phenomenon, we refer to this as coherent scatter. Dark hole speckle noise is caused by scatter from long spatial frequencies (Table B-1).

Table B-1: Long Spatial Frequency Errors that Scatter into Dark Hole

Scatter Angle [mas]	PSD Spatial Frequency [1/µm] for λ = 600 nm	Spatial Period [m]	Cycles per 6-m Aperture
30	2.5×10^{-7}	4	1.5
60	5×10^{-7}	2	3
200	1.7×10^{-6}	.6	10
600	5×10^{-6}	0.2	30

According to R-R **[B-2]**, the ratio of power in first diffraction order (at a given angle for a given wavelength) to incident power (i.e. flux ratio) is given by:

$$\frac{P_{\pm 1}}{P_i} = \left(\frac{2\,\pi\,a}{\lambda}\right)^2 \cos\theta_i \cos\theta_{\pm 1}$$

Where a = peak-valley amplitude of the sinusoid. For incidence and scatter angles smaller than 0.1 rad (~ 5 deg), the cosine terms are unity. Thus, the scattered light across the dark hole is essentially flat and the required peak amplitude stability is proportional to wavelength.

$$a = \sim \left(\frac{\lambda}{2}\right) x\, 10^{-6}$$

B.2.2 Generalized Harvey-Shack (GHS) Surface Scatter Theory

Generalize Harvey-Shack (GHS) surface scatter theory is a parametric or 'scalar' theory that provides accurate predictions for moderate-amplitude randomly rough surfaces at arbitrary incident and scatter angles. **[B-6]** GHS theory models BRDF and is described by three parameters, Slope S, Knee L and Peak b_0 (**Fig B-4**) **[B-7]**:

$$BRDF(\theta) = b_0 \left[1 + \left(\frac{\theta}{L}\right)^2\right]^{S/2}$$

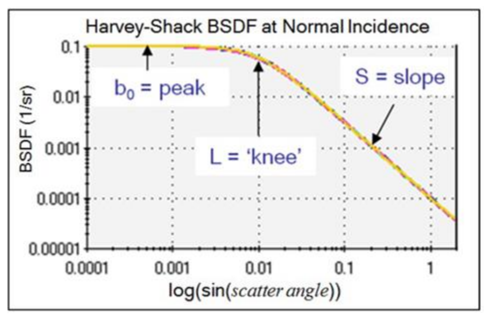

Fig. B-4: Parametric variables that describe Harvey-Shack scatter function for a smooth optical surface. **[B-7]**

The b_0 parameter is the near-specular (peak) BRDF and because the angles are so small, its value is constant for all angles across the coronagraph's dark hole. The S parameter is the power-law falloff of the surface's PSD. S is how smooth the mirror is polished and typically varies from -2 to -3. The L parameter is the angle at which BRDF transitions from a power-law falloff to a constant Lambertian value (i.e. angle at which scatter becomes a constant incoherent background).

B.3 BRDF, PSD and Near-Angle Scatter Throughput

Bidirectional Reflectance Distribution Function (BRDF) (defined by Nicodemus in 1977 **[B-8]**) is a geometric relationship to describe surface scatter in radiometric terms. (**Fig B-5**) BRDF is defined as the reflected radiance, L, (power per unit solid angle per unit projected area) divided by the incident irradiance, E, (power per unit area). **[B-2, B-9]** (Please note that the international standard (SI) radiometric irradiance E notation is different from electric field E vector.)

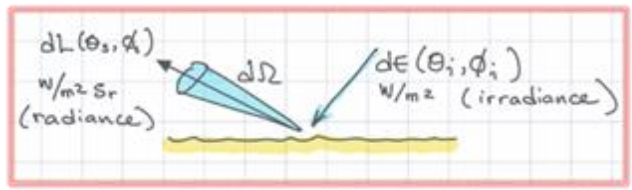

Fig B-5: BRDF Defining Geometry

$$BRDF\,(\theta_s,\,\varphi_s;\,\theta_i,\,\varphi_i) = \frac{dL\,(\theta_s,\,\varphi_s;\,\theta_i,\,\varphi_i)}{dE\,(\theta_s,\,\varphi_s;\,\theta_i,\,\varphi_i)} = \frac{\Phi_s/\Omega}{\Phi_i cos\,(\theta_s,\varphi_s)} = \frac{\Phi_s/\Omega}{\Phi_i}$$

where:

Φ_i = Total Power Incident on Entrance Pupil, i.e. Primary Mirror Area, = $E_i \, x \, A_{PM}$
Φ_s/Ω = Power per unit Solid Angle Scattered from Entrance Pupil, i.e. PM Area
$\Omega = \pi\,(\lambda/D)^2$ = Solid Angle of the Primary Mirror's PSF
λ = Wavelength
D = Primary Mirror Diameter
$(\theta_s, \varphi_s; \theta_i, \varphi_i)$ = (Nλ/D, Nλ/D; 0, 0) where N = 1 to 30 so that (θ_s, φ_s) are very small

BRDF is frequently plotted in $(\beta - \beta_0)$ space where $\beta = \sin(\theta_s)$, $\beta_0 = \sin(\theta_i)$. Thus, the scattered power from the PM, directly imaged into a dark hole pixel is given by:

$$\Phi_s(u,v)_{Core} = \mathrm{BRDF}(\lambda/D < (\beta - \beta_0) < N\lambda/D) \cdot \Phi_i \cdot \Omega_{Core}$$

BRDF is also mathematically equivalent to the surface's PSD **[B-2]**:

$$\mathrm{PSD}(f_x,\,f_y) = \left[\frac{10^8\,\lambda^4}{16\pi^2}\right] \cdot \mathrm{BRDF}(\beta - \beta_0)\ [\text{Å}^2\ \mu\text{m}^2]$$

For small angles, the equation simplifies to PSD_0 and $BRDF_0$, because both are constant across the dark hole.

$$\mathrm{PSD}_0 = \left[\frac{10^8\,\lambda^4}{16\pi^2}\right] \cdot \mathrm{BRDF}_0\ [\text{Å}^2\ \mu\text{m}^2]$$

Finally, BRDF provides a direct method to calculate Near-Angle Scatter Throughput of contrast leakage (as defined in Appendix A):

$$\tau_{NAS} \equiv \frac{\Phi_s}{\Phi_i} = BRDF\ d\Omega = BRDF \cdot \pi \left(\frac{\lambda}{D}\right)^2$$

B.4 Power Spectral Density

Given that both Rayleigh-Rice and Harvey-Shack models use surface BRDF scatter function or PSD structure functions, and, given that both these expressions can directly give NAS Throughput, it is important to spend some time with the mathematics of PSD. Particularly given how PSD can inform both correlated (i.e. angular) and uncorrelated (i.e. diffuse) scatter.

B.4.1 Surface Power Spectral Density (PSD) and Auto-Covariance Function (ACF)

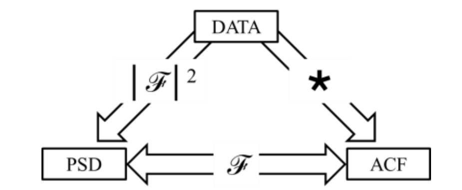

Fig. B-6: PSD is modulus square of data set Fourier transform or Fourier transform of data set's autocovariance function.

PSD decomposes any data set into contributions per frequency (spatial or temporal). The PSD of a data set can be calculated two ways: either by taking the modulus square of the Fourier transform of the data set, or by taking the Fourier transform of the autocovariance function (ACF) of the data set. (**Fig B-6**) The ACF of a data set is calculated by taking its autoconvolution, i.e., shearing the data set against itself.

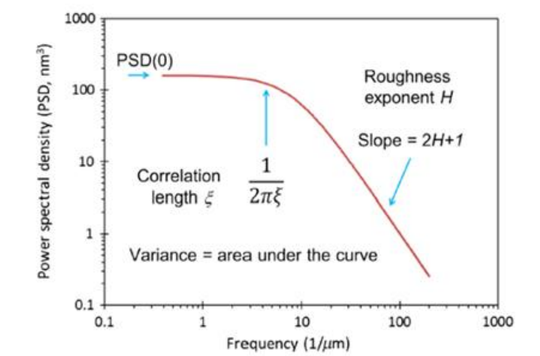

Fig. B-7: Graphical representation of PSD. **[B-10]**

A typical PSD is described by three parameters: PSD(0) (zero-frequency value of PSD); correlation length, ℓ; and the roughness exponent H (for Hurst). (**Fig B-7**) **[B-10]** For optical surfaces, the PSD to the 'right' of the correlation length cutoff falls off as a statistical function with negative slope. For polished surfaces this slope is typically between -2 and -3. This region of the PSD describes the surface's structure that can be decomposed into correlated spatial frequencies – spatial frequencies which scatter light into discrete angles via the grating equation. The PSD to the 'left' of the correlation length cutoff is flat because at these spatial frequencies surface structure is uncorrelated. Thus, these spatial frequencies scatter light diffusely into all angles. As a reminder, the PSD of an ideal Lambertian surface is simply a flat line for all spatial frequencies. Obviously, correlation length is important.

B.4.2 Correlation Length

Correlation Length (ℓ) is the maximum shear for which the surface spatial structure is correlated (i.e., the longest spatial wavelength Fourier decomposed periodic component). Surface structure separated by a distance larger than the correlation length are statistically independent, i.e., uncorrelated. Some define ℓ to be where the ACF equals zero, others define it as where the ACF equals 1/e. It is important to understand that the correlation length calculated from a data set is 'band limited'. If the surface is smooth, then the limit is either L or L/2 where L = sample length (depending on how correlation length is defined). If the surface is not smooth, then the limit might be shorter.

B.4.3 Band limited Data

The problem with calculating PSD (and ACF) from measured surface data is that no single instrument can cover the entire frequency range. Measured data is band-limited, therefore, calculations of PSD (and ACF) are band-limited. (**Fig. B-8**) The longest spatial period (lowest spatial frequency) is limited by sample length. The shortest spatial period (highest spatial frequency) is limited by pixel size and Nyquist spacing. Interferometers and micro-profilometers can measure from one cycle across their data set (maybe half cycle) to a few hundred cycles. Interferometers typically measure a surface's full aperture. While micro-profilers (and sub-aperture interferometers) sample the surface. Micro-profilers measure areas of a few millimeters. Each instrument provides a band-limited measured RMS roughness estimate:

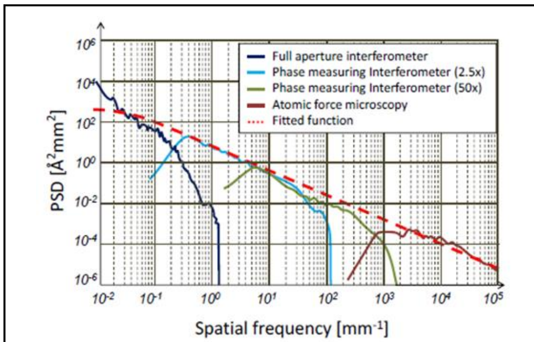

Fig. B-8: Measured PSD is band-limited. **[B-11]**

$$\sigma = \left[\int_{f_1}^{f_2} PSD(f)df\right]^{1/2}$$

Total RMS roughness for the surface is obtained by calculating the root-sum-square (RSS) of the the band-limited estimates:

$$\sigma^2_{Total} = \sigma^2_{Low} + \sigma^2_{Mid} + \sigma^2_{High}$$

While it is well known that instruments are band-limited in their measurement of surface statistics, what is less well known is how these band-limited estimates impact near angle scatter. The answer requires a somewhat complicated but linear development. First, if PSD is band-limited, then so is ACF. The total ACF of a surface is the summation of individual band limited ACFs. Each instrument produces its own ACF with its own band-limited estimate of RMS roughness and correlation length. (**Fig B-9**) It is important to understand that the correlation length of a given measurement may be due to the instrument's limitation and not the surface statistics. For example, the low and mid-spatial frequency correlation length due to the instrument's band limits and not the surface.

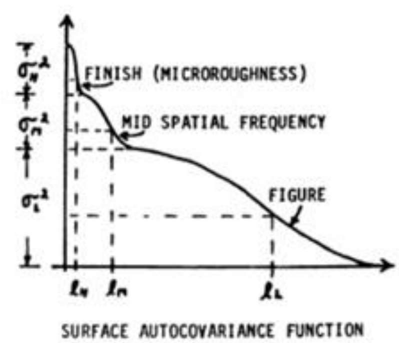

Fig. B-9: As PSDs are band limited, so are ACFs, and each has their own correlation length. **[B-12]**

Next, a surface's total PSD (or PSF) is a stack of their band-limited estimates. (**Fig B-10 & Fig B-11)** The reason is because no single instrument can measure the scattered light caused by surface structure outside of its band limits.

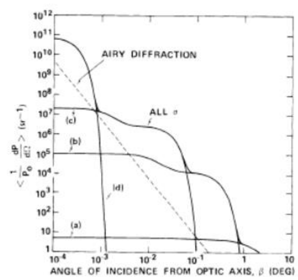

Fig. B-10: Angle Resolved Scatter (ARS) vs angle of incidence. Dotted line is Airy Diffraction envelope. Solid lines are scattered light. **[B-13]**

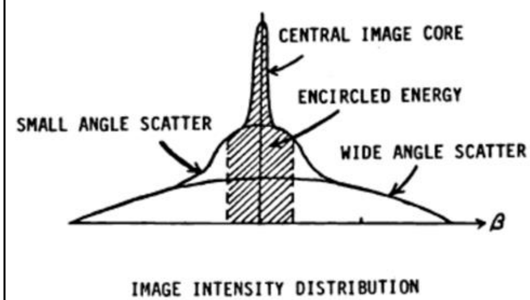

Fig. B-11: Point Spread Function (PSF) is sum (stack) of diffraction and scatter. **[B-12]**

So, what does this mean for near-angle scatter? The answer is: even if one removes all a mirror's correlated low- and mid-spatial frequency surface structure, either via computer-controlled polishing or a deformable mirror, the surface will always have some amount of microstructure. And, while the spatially correlated portion of this microstructure scatters (diffracts) light into large angles, the spatially uncorrelated portion of this microstructure diffusely scatters light into all angles, including angles very close to the specular reflection. (**Fig B-12**)

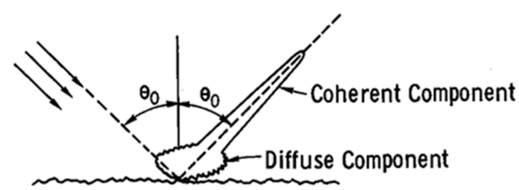

Fig. B-12: Scatter consists of large coherent component and small diffuse component. **[B-14]**

B.4.4 Importance of Correlation Length and Distribution Functional Form

While typically overlooked, Correlation Length (ℓ) may be the most important parameter for Near-Angle Scatter. According to Beckmann-Kirchhoff theory **[B-2]**, for an isotropic random surface with normal (Gaussian) height distribution much smaller than the illuminating wavelength and a Gaussian autocorrelation function, the PSD is determined by a surface's microstructure rms roughness, σ, and correlation length, ℓ,

$$\mathrm{PSD}_{2D}(f) = \pi\, \ell^2\, \sigma^2\, e^{-(\pi \ell f)^2},$$

where f is spatial frequency. Thus, the amplitude of the near-angle 'Lambertian' scatter is given by $\mathrm{PSD}_{2D}(0) = \pi\, \ell^2\, \sigma^2$. **Fig B-13** shows that for two surfaces with the same RMS roughness, the surface with the longer correlation length (i.e. the smoother surface) has a higher $\mathrm{PSD}_{1D}(0)$. Thus, this surface will have higher near-angle scatter.

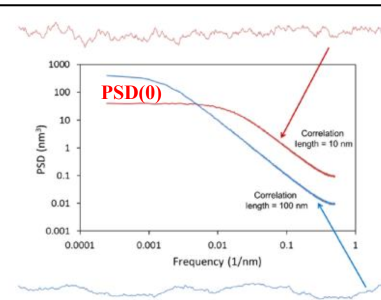

Fig. B-13 $\mathrm{PSD}_{1D}(0)$ depends on roughness and correlation length. **[B-10]**

More generally, PSD is often represented by an inverse power law model,

$$PSD_{2D}(f) = \frac{KAB}{[1 + (Bf)^2]^{(C+1)/2}},$$

where:

$$PSD_{2D}(0) = KAB = \frac{C-1}{2\pi}(B\sigma)^2 \quad \text{if } C > 1.$$

In the case of $C = 2$, the PSD profile is Lorentzian. Thus, from the inverse Fourier transform, the ACV is a decaying exponential, and B is the 1/e correlation length. In the case where $C = 2\pi^2 + 1$, the equation for $PSD_{2D}(0)$ profile is Gaussian and $B = \ell$. Note that the Gaussian case has a $PSD_{2D}(0)$ that is a factor $(2\pi^2 + 1)/2$ greater than the Lorentzian case, given the same values of B and σ. **[B-15]**

B.5 Total Integrated Scatter (TIS) and Near-Angle Scatter Throughput

Total Integrated Scatter (TIS) is another scatter metric that has relevance to Scatter Throughput. There are multiple methods to quantify TIS. **[B-2]** Assuming perfect reflectance, TIS can be defined as the ratio of total hemispherical scattered flux to total incident flux.

$$TIS = \frac{\Phi_s}{\Phi_i}$$

Mathematically, it is the integral of BRDF over the full projected hemispherical solid angle.

$$TIS = \iint BRDF \; d\Omega$$

TIS is typically quantified experimentally with an integrating sphere by reflecting an incident beam off a sample and measuring the total power on to the sample, the power in the reflected specular beam and the diffuse scatter. (**Fig B-15**) The diffuse scatter component is related to surface roughness.

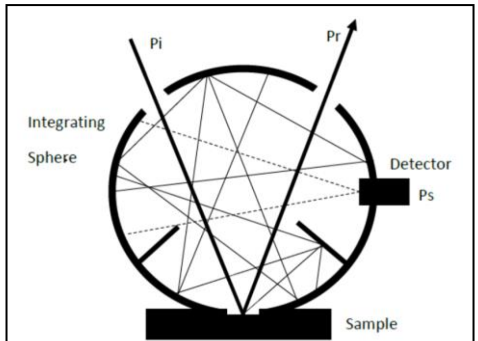

Fig. B-15 Diffuse Total Integrated Scatter Measurement. **[B-16]**

$$TIS_{diffuse} = \left(\frac{4\pi\,\sigma}{\lambda}\cos\theta\right)^2$$

For near-angle, the cosine term goes to 1.

TIS can be used to estimate the near-angle diffuse scatter throughput in the dark hole by multiplying TIS by the primary mirror's PSF solid angle

$$\tau_{NAS} \equiv \frac{\Phi_{S_{core}}}{\Phi_i} = \frac{\Phi_s}{\Phi_i}\, d\Omega = TIS\, d\Omega$$

APPENDIX B: REFERENCES

B-1 Harvey, James & Kotha, Anita. (1995). Scattering effects from residual optical fabrication errors. Proceedings of SPIE - The International Society for Optical Engineering. 155-174. 10.1117/12.215588.

B-2 Stover, John C, Optical Scattering Measurement and Analysis, Third Edition, SPIE Press, 2012

B-3 1. James E. Harvey, Narak Choi, Andrey Krywonos, Gary L. Peterson, Marilyn E. Bruner, "Image degradation due to scattering effects in two-mirror telescopes," Opt. Eng. 49(6) 063202 (1 June 2010) https://doi.org/10.1117/1.3454382

B-4 J. M. Elson, J. M. Bennett, "Vector Scattering Theory," Opt. Eng. 18(2) 182116 (1 April 1979) https://doi.org/10.1117/12.7972336

B-5 Sven Schröder, Marcus Trost, Torsten Feigl, James E. Harvey, Angela Duparré, "Efficient specification and characterization of surface roughness for extreme ultraviolet optics," Proc. SPIE 7969, Extreme Ultraviolet (EUV) Lithography II, 79692C (8 April 2011); https://doi.org/10.1117/12.891280

B-6 Narak Choi, James E. Harvey, "Numerical validation of the generalized Harvey–Shack surface scatter theory," Opt. Eng. 52(11) 115103 (26 November 2013) https://doi.org/10.1117/1.OE.52.11.115103

B-7 Richard N. Pfisterer, James E. Harvey, James B. Breckinridge, "The role of narrow-angle forward surface scatter and particulate scatter in exoplanet exploration," Proc. SPIE 10698, Space Telescopes and Instrumentation 2018: Optical, Infrared, and Millimeter Wave, 106985F (6 July 2018); https://doi.org/10.1117/12.2314229

B-8 Nicodemus, F. E, et al., “Geometric Considerations and Nomenclature for Reflectance”, US Dept of Commerce, Washington DC, NBS Monograph 160, 1977.

B-9 Harvey, James E, Understanding Surface Scatter Phenomena a Linear Systems Formulation, SPIE Press, 2019

B-10 Chris A. Mack, "Reducing roughness in extreme ultraviolet lithography," J. Micro/Nanolith. MEMS MOEMS 17(4) 041006 (7 August 2018) https://doi.org/10.1117/1.JMM.17.4.041006

B-11 Narak Choi, James E. Harvey, "Linear systems formulation of image analysis in the presence of both aberrations and surface scatter," Proc. SPIE 8128, Current Developments in Lens Design and Optical Engineering XII; and Advances in Thin Film Coatings VII, 81280B (7 September 2011); https://doi.org/10.1117/12.910930

B-12 William P. Zmek, Edward C. Moran, James E. Harvey, "The Effects Of Surface Quality Upon The Performance Of Normal Incidence X-Ray/XUV Imaging Systems," Proc. SPIE 0984, X-Ray Multilayers in Diffractometers, Monochromators, and Spectrometers, (16 December 1988); https://doi.org/10.1117/12.948788

B-13 J. M. Elson, H. E. Bennett, "Image Degradation Caused By Direct Scatter From Optical Components Into The Image Plane," Proc. SPIE 0511, Stray Radiation IV, (17 January 1985); doi: 10.1117/12.945028

B-14 Allen, Chris, “Surface Scattering”, Course website URL people.eecs.ku.edu/~callen/823/EECS823.htm

B-15 Eugene L. Church and Peter Z. Takacs "Optimal estimation of finish parameters", Proc. SPIE 1530, Optical Scatter: Applications, Measurement, and Theory, (1 December 1991); https://doi.org/10.1117/12.50498

B-16 John C. Stover and Christian N Staats, “RMS Roughness, Total Integrated Scatter and Fractional Scatter of Production Parts”, The Scatter Works, Inc. https://thescatterworks.com/wp-content/uploads/TI-and-FS-measuremnets.pdf

Disclosures

The authors declare that there are no financial interests, commercial affiliations, or other potential conflicts of interest that could have influenced the objectivity of this research or the writing of this paper. All the work reported here has been conducted under the leadership and guidance of the authors and some other NASA subject matter experts. Both authors were NASA Civil Servants during these activities and they were subjected to strict institutional procurement acquisition regulations (Federal Acquisition Regulations, FAR) and ethical practices.

Code and Data Availability

No code or materials were used in preparing this paper. The analysis used some data that are partially publicly available.

Acknowledgments

This work was initiated upon the request of Dr. James Breckinridge to look into "how near angle scatter might impact exo-Earth coronagraphy". It was performed under NASA Engineering and Safety Center (NESC) Assessment TI-22-01811, titled "Specifying Optical Surfaces to Control Near-Angle Scatter at <100 milli-arcseconds" managed by the NESC Sensors and Instrument Technology Discipline Team Leads Upendra Singh and Jessica Gaskin. It was funded by both the NESC and the NASA Astrophysics Division's Internal Scientist Funding Model. This paper merges multiple previously published SPIE conference proceedings with the NESC final report and new content created during manuscript preparation into a single whole. This paper benefited significantly from contributions subject matter expert collaborators (Bijan Nemati, Tellus1; Scott Ellis and Richard Pfister, Photon Engineering; Mateo Batkis, Javier Del Hoyo, Manuel Quijada, and Luis Rodriguez, GSFC; and John Stover, Scatterworks), independent technical reviewers (Nick Siegler and Pin Chen, ExEP; John Krist, Charles Noecker, and Stuart Shaklan, JPL; and Ed Wollack, GSFC), and institutional reviewers from the NESC Chief Engineer's Office.

H. Philip Stahl, senior optical physicist at NASA MSFC, is a leading authority in optical systems engineering and metrology. He matures mirror technology for large space telescopes including the Webb Telescope and authors the ‘Stahl’ telescope cost model. He is recipient of NASA’s Distinguished Service Medal; Fellow of SPIE and OSA; and SPIE 2014 President. He earned PhD (1985) and MS (1983) in Optical Science at University of Arizona and BA (1979) in Physics/Mathematics at Wittenberg University.